Super-enhancer-driven ZFP36L1 promotes PD-L1 expression in infiltrative gastric cancer

Xujin Wei[1,2,3†], Jie Liu[1†], Jia Cheng[2,3], Wangyu Cai[2,3], Wen Xie[2,3], Kang Wang[2,3], Lingyun Lin[2,3], Jingjing Hou[2,3], Huiqin Zhuo[2,3*], Jianchun Cai[1,2,3*]

[1]The Graduate School of Fujian Medical University, Fuzhou, Fujian, China

[2]Department of Gastrointestinal Surgery, Zhongshan Hospital of Xiamen University, Institute of Gastrointestinal Oncology, School of Medicine, Xiamen University, Xiamen, Fujian, China

[3]Xiamen Municipal Key Laboratory of Gastrointestinal Oncology, Xiamen, Fujian, China

[†]Contribute equally to this work

***Correspondence:**

Huiqin Zhuo
zhuohuiqin@xmu.edu.cn

Jianchun Cai
caijianchun@xmu.edu.cn

Abstract

Gastric cancer (GC) is a major cause of cancer-related mortality worldwide. Despite the widespread recognition of tumor immunotherapy in treating unresectable GC, challenges, including ineffective immunotherapy and drug resistance, persist. Therefore, understanding the regulatory mechanisms of PD-L1, particularly in the context of super-enhancers (SEs) and zinc finger protein 36 ring finger protein-like 1 (ZFP36L1) RNA-binding protein, is crucial.

Methods: In this study, we performed H3K27ac CUT&Tag sequencing, investigated the heterogeneity of SEs between two GC subtypes with differential growth patterns, and revealed the immune escape signatures driven by ZFP36L1-SE in infiltrative GC through SEs inhibitors treatment. The regulation of ZFP36L1 to PD-L1 was evaluated by quantitative PCR, western blot, flow cytometry and immunohistochemistry. Furthermore, we explored its regulatory mechanisms using a combination of molecular biology techniques, including luciferase reporter assay, GST/RNA pull-down, ChIP/RIP experiments, and in vivo functional assays.

Results: We demonstrated that ZFP36L1, driven by an SE, enhances IFN-γ-induced PD-L1 expression, with SPI1 identified as the specific transcription factor binding to ZFP36L1-SE. Mechanistically, ZFP36L1 binds to the adenylate uridylate-rich element in the 3′UTR of *HDAC3* mRNA, exacerbating its mRNA decay, and thereby facilitating PD-L1 abnormal transcriptional activation.

Conclusions: Collectively, our findings provide mechanistic insights into the role of the SPI1–ZFP36L1–HDAC3–PD-L1 signaling axis in orchestrating immune escape mechanisms in GC, thereby offering valuable insights into the potential targets for immune checkpoint therapy in GC management.

Keywords: stomach neoplasm, Ming classification, super enhancer, PD-L1, mRNA decay.

Introduction

Gastric cancer (GC) remains the third leading cause of cancer-related mortality in China, thereby posing significant socio-economic challenges [1]. The Ming classification, which categorizes GC into infiltrative and expanding subtypes based on distinct growth patterns, is pivotal in understanding the biological heterogeneity of this disease [2]. Tumor immunotherapy, particularly targeting programmed cell death 1 ligand 1 (PD-L1; CD274), is a promising approach for unresectable GC [3]. Notably, PD-L1, expressed on tumor cell surfaces, interacts with PD-1 receptors on cytotoxic T cells, leading to T-cell apoptosis and facilitating cancer immune evasion. Clinical studies, such as KEYNOTE-811, have demonstrated the efficacy of PD-L1 inhibitors, including pembrolizumab, especially in HER2-positive gastric adenocarcinoma study [4]. Therefore, current guidelines recommend the use of checkpoint inhibitor therapy in GC cases with high PD-L1 combined positive scores. Despite these advancements, elucidating the regulatory mechanisms of PD-L1 is imperative owing to challenges associated with ineffective immunotherapy and drug resistance.

Super-enhancers (SEs), initially proposed by Richard A. Young, are densely clustered transcriptionally active enhancers [5]. SEs exhibit distinct characteristics, including heightened enrichment of histone H3 acetylation at lysine 27 (H3K27ac), recruitment of numerous transcription factors (TFs) such as bromodomain-containing protein 4 (BRD4), MED1, and P300, and robust stimulation of target genes. Utilizing the Rank Ordering of Super-Enhancers (ROSE) algorithm, researchers can identify and explore cancer-associated SEs through techniques such as ChIP-seq and Cleavage Under Targets and Tagmentation (CUT&Tag) [6]. In the epigenetic landscape of tumors, acquired SEs are implicated in promoting transcriptional dysregulation, contributing to oncogenesis, invasion, metabolic alterations, drug resistance and the establishment of an immunosuppressive microenvironment [7, 8]. Previous studies have elucidated the unique SE landscape in mesenchymal-type GC and highlighted the role of EMT-related kinase NUAK1 at both transcriptional and epigenetic levels [9]. However, further investigations are warranted to elucidate the effects of SEs during GC metastasis and immune evasion.

The Zinc-finger protein 36 (ZFP36) gene family encodes three RNA-binding proteins: ZFP36, ZFP36L1, and ZFP36L2, characterized by two CCCH-type tandem zinc finger domains. These proteins recognize adenylate uridylate-rich elements (AREs) in the 3′ untranslated region (UTR) of target mRNAs, leading to mRNA deadenylation and degradation, ultimately diminishing protein synthesis. ZFP36 targets multiple inflammatory factors thereby playing a crucial role as an anti-inflammatory factor closely associated with inflammatory diseases such as psoriasis and arthritis [10]. *ZFP36L2* has been identified as an SE-activated gene with proto-oncogenic functions in GC [11]. *ZFP36L1*, also known as *TIS11B*/*BRF1*, is primarily located in the q24.1 region of human chromosome 14, with a length of 8599 bases long. The gene exhibits three annotated transcripts, with NM_004926.4 being the predominant transcript. The encoded protein comprises 338 amino acids and contains two tandem zinc finger structural domains, a nuclear localization signal, and a nuclear export signal region. It is distributed across the nucleus, cytoplasm, and subcellular structural apparatus. Despite ongoing debates regarding its role, ZFP36L1 remains a subject of interest in tumor biology.

We previously identified differential protein expression patterns in expanding and infiltrative GC, notably observing increased levels of MED1 and P300 in infiltrative GC **(Supplementary**

Figure 1A) [12]. Based on these findings, we postulated that infiltrative GC may exhibit heightened enhancer activity and dysregulated transcription. To validate this hypothesis, we aimed to compare the distribution of SEs between Ming-expanding and infiltrative GC. ZFP36L1-SE was then identified as the key SE in infiltrative GC. Additionally, we aimed to elucidate the significance of SE-driven ZFP36L1 in tumor immune evasion and the SPI1–ZFP36L1–HDAC3–PD-L1 signaling axis. Collectively, we believe that our findings would contribute to a deeper understanding of immune checkpoint therapies for GC.

Materials and Methods

Cell lines and tissues

MKN45, MGC803, 293T, and MC38 were acquired from the Institute of Cell Biology (Shanghai, China). Infiltrative GC cell line XGC-1 (China patent No.CN103396994A) and expanding GC cell line XGC-2 (China patent No.CN103387963B) were constructed by our team [13, 14]. 293T and MC38 were grown in high-glucose DMEM with 10% FBS, and other cell lines were cultured in RPM1640 medium. Six GC tissues for H3K27ac CUT&Tag sequencing were obtained from patients undergoing resection of primary GC at the Zhongshan Hospital of Xiamen University. GC tissue microarray (HStmA180Su19) containing 70 PD-L1 positive cancer tissues was acquired from Outdo Biotech (Shanghai, China).

Bioinformatic analysis

Bioinformatics analyses and graphing of experimental results were performed using R (4.2.1) version, involving the following R packages: ggplot2 [3.3.6] car [3.1-0], and stats [4.2.1] for histograms, GOSemSim [2.22.0] for Friends analysis, VennDiagram [1.7.3], clusterProfiler [4.4.4] for GO-KEGG analysis, survival [3.3.1] and survminer for Kaplan-Meier survival curves, ConsensusClusterPlus for unsupervised clustering, ggalluvial [0.12.3] for Sankey diagram, circlize [0.4.15] for the localization maps, ggwordcloud [0.6.0] for word cloud. The Rank Ordering of Super-Enhancers (ROSE) algorithm: http://younglab.wi.mit.edu/super_enhancer_code.html. Primer design was performed using Primer Premier 5. Mechanism mapping: http://gdp.renlab.cn .

CUT&Tag and chromatin immunoprecipitation (ChIP)

Epi™ CUT and Tag Kit (Epibiotek, Guangzhou, China) was used to perform the CUT&Tag experiment with 5 steps: mixing the cell suspension with magnetic beads (10 μL ConA Beads and 1×10^5 cells), antibody binding (297 μL Wash Buffer, 3 μl 5% Digitonin, 12 μL 25× pAb Mix, and 3 μL antibody), incubation with Pa-Tn5 transposome, labeling (50 μL Tagmentation Buffer for 1 h at room temperature), library construction and sequencing. ROSE algorithm was programmed in Python (v3.9) to identify SEs. The data was visualized using IGV 2.14.1.

Sonication ChIP Kit (ABclonal, Wuhan, China) was used to perform the ChIP experiment with 5 steps: crosslinking (1% formaldehyde solution 10 min, 10×Glycine Solution 5 min), cell nuclear extraction (1×10^7 cells, centrifugation at 5000 ×g for 5 min at 4°C), ultrasonication (25% power with 3-second on/off periods for a total of 8 min, ideal fragment size: 200-500 bp), immunoprecipitation, eluting the chromatin, de-crosslinking, DNA purification and qPCR. The primary H3K27ac antibody (ABclonal, Cat.No.A7253) or SPI1 antibody (Abcam, Cat. No. ab227835) was used at 10 ug per sample. Primer sequences are available in **Supplementary Table 1**.

Western blot

Antibodies used for the western blot assay were as follows: ZFP36L1(Abcam, Cat. No. ab230507); HDAC3 (Abcam, Cat. No. ab76295); CD274 (Proteintech, Cat.No.66248-1-lg); HA-Tag (Proteintech, Cat.No.51064-2-AP); DDDDK-Tag (ABclonal, Cat.No.AE005); β-actin (ABclonal, Cat.No.AC026).

Dual-luciferase reporter assay

293T cells in 12-well plates were transfected with 0.8 μg *Renilla* luciferase plasmid, 0.8 μg firefly luciferase plasmid (vector: pGL4 or pmirGLO) and 0.8 μg TF plasmid. Dual-luciferase reporter assay kit (Vazyme, Nanjing, China) was used to detect the enzyme/substrate reactions, and the fluorescence values were normalized.

Flow cytometry

1×10^6 cells was washed and resuspended in 100 μL FACS buffer (98% PBS + 2% FBS) after digestion. 1 μL fluorescently-labeled primary CD274 antibody (ABclonal, Cat.No.A22305) was added per tube and incubated for 20 minutes at room temperature. Cells labeled for PD-L1 were detected by flow cytometry (excitation light: 647 nm; emission light: 664 nm) and the data was visualized using FlowJo (v10.8.1).

Actinomycin D induced mRNA decay

Cells were seeded in 6-well plates and allowed to grow to 80%. Add actinomycin D to a final concentration of 1 μg/mL, and cellular RNA in each plate was collected every other hour. RNA extraction was performed using the FastPure Cell/Tissue Total RNA Isolation Kit (Vazyme, Nanjing, China), and Real-Time PCR was performed using UltraSYBR Mixture (Cowin Biotech, Jiangsu, China).18s rRNA was used as an internal reference gene, and half-lives were calculated from linear-log graphs.

Animals and treatment

5-week C57BL/6J or BALB/c mice were purchased from Xiamen University Laboratory Animal Center, and the center was responsible for the daily feeding. At the beginning of each experiment, all mice were randomly assigned to control or experimental groups each containing six mice. MC38 cells were infected with shZFP36L1 expression lentivirus, and 2×10^6 cells were injected subcutaneously or 1×10^6 cells were injected into the tail vein. Two weeks later, mice were sacrificed and dissected for the hematoxylin & eosin (HE) and immunohistochemical (IHC) staining.

Results

SE heterogeneity between two subtypes of gastric cancer with differential growth patterns

Six GC samples were collected, and H3K27ac CUT&Tag sequencing was performed for the first time to identify of GC SEs **(Figure 1A)**. The two GC growth patterns did not significantly differ in terms of typical enhancers **(Supplementary Figure 1B)**. However, a bimodal H3K27ac enrichment was observed in infiltrative GC compared with that in expanding GC **(Figure 1B)**. A total of 1057 and 819 infiltrative and expanding SE peaks, respectively, were obtained using the ROSE algorithm. Over 50% of these peaks were located in the non-coding regions such as exons and introns, and their predicted target genes were transcribed to produce non-coding RNAs; the peaks distributed in transcription start and termination sites activated the promoters and directly drove the

transcription of protein-coding genes **(Figure 1C)**. Collectively, these data targeted 240 infiltrative and 173 expanding SE-driven genes **(Figure 1D, Supplementary Figure 1C)**.

Gene Ontology (GO) and Kyoto Encyclopedia of Genes and Genomes (KEGG) analyses displayed that negative regulation of T cell proliferation, response to tumor necrosis factor (TNF), regulation of epithelial cell migration and 3′UTR-mediated mRNA destabilization pathway signatures were enriched in infiltrative SE-driven genes **(Figure 1E)**. Sixteen of these infiltrative SE-driven genes had value in The Cancer Genome Atlas (TCGA) datasets **(Supplementary Figure 1D)**. Unsupervised hierarchical clustering revealed that infiltrative SE-driven clusters showed significant infiltration of memory, regulatory, and helper T cells **(Figure 1F–H)**. The protein expression present in 70 PD-L1 positive GC tumor tissues was assessed, and high immunohistochemistry (IHC) scores were determined in PD-L1 infiltrative GC compared with those in expanding GC **(Figure 1I)**. These results helped describe the SE-driven immune escape signatures of infiltrative GC.

ZFP36L1 **as an SE-driven oncogene in infiltrative GC**

ZFP36L1 was selected among these 16 genes based on Friends analysis and a comprehensive exploration of the TCGA data **(Figure 2A)**. The mRNA expression in GC correlated positively with high T stage, tumor grade, diffuse type, and *Helicobacter pylori* infection **(Figure 2B)** and negatively correlated with overall survival, disease-specific survival and progression-free interval **(Supplementary Figure 1E)**. Notably, high *ZFP36L1* expression represented high Tumor Immune Dysfunction and Exclusion (TIDE) scores, T-cell infiltration and high CD274 expression **(Figure 2C–E)**. Therefore, we speculated that ZFP36L1 is a key molecule for immune escape in infiltrative GC, and ZFP36L1-SE (chr14:68806839–68816867) is a probable cause of transcriptional dysregulation as it is situated upstream of the *ZFP36L1* promoter **(Figure 2F, G)**. This genomic region harbors two typical enhancers (E1:68806839–68807740 and E2:68816088–68816867) and shows a plethora of histone acetylation enrichments in infiltrative GC tissues, as well as in MKN45 and AGS cell lines. A similar trend was observed at the protein level in this study. In the 12 paired infiltrative GC samples, ZFP36L1 protein expression was higher in 10 primary neoplasms than that in normal adjacent tissues **(Figure 2H)**. Additionally, various GC cell lines exhibited high ZFP36L1 expression compared with that in the normal gastric epithelial cell line, GES-1 **(Figure 2I)**.

To validate whether ZFP36L1 was driven by the SEs, XGC-1 and MKN45 cells were treated with the SE inhibitors THZ1 and JQ1. We observed that THZ1 and JQ1 inhibited mRNA and protein expression of ZFP36L1 in a concentration- and time-dependent manner, respectively **(Figure 2J)**. Moreover, ChIP experiments revealed that JQ1 decreased H3K27ac enrichment in ZFP36L1-SE region, especially in E1 region **(Figure 2K)**. These findings suggest that *ZFP36L1* is a key SE-driven oncogene involved in infiltrating GC.

ZFP36L1 promotes IFN-γ-induced PD-L1 expression

Given the aforementioned results, we speculated that ZFP36L1 contributes to heightened PD-L1 expression in infiltrative GC. Typically, IFN-γ derived from T cells triggers PD-L1 overexpression on the surface of GC cells. In vitro experiments were conducted to simulate the immune microenvironment by adding exogenous IFN-γ at a concentration of 40 ng/mL, exacerbating PD-L1 expression on GC cells. However, in *ZFP36L1*-knockdown XGC-1 and MKN45 GC cell lines, IFN-γ-induced PD-L1 transcription levels were lower compared with that in the control group **(Figure 3A)**. Conversely, we observed a significant increase in IFN-γ-induced PD-L1 mRNA expression in XGC-2 and MGC803 cell lines overexpressing *ZFP36L1* **(Figure 3B)**. These results indicate that ZFP36L1 potentiates IFN-γ-induced PD-L1 transcription.

At the protein level, knocking down *ZFP36L1* in the XGC-1 and MKN45 cell lines similarly reduced IFN-γ-induced PD-L1 protein expression **(Figure 3C)**. Conversely, overexpression of *ZFP36L1* in the XGC-2 and MGC803 cell lines facilitated IFN-γ-induced PD-L1 protein expression **(Figure 3D)**. Flow cytometry revealed a consistent trend in the expression levels of PD-L1 on the tumor cell membrane surface. Knockdown of *ZFP36L1* decreased the surface PD-L1 fluorescent signal in IFN-γ-induced XGC-1 and MKN45 cells compared with that in the control group **(Figure 3E)**, whereas overexpression of ZFP36L1 demonstrated a higher fluorescent signal intensity in IFN-γ-induced XGC-2 and MGC803 cells **(Figure 3F)**. These results validate the conclusion that ZFP36L1 expression is positively correlates with IFN-γ-induced PD-L1 expression at the protein level.

SPI1 binding to the SE region of *ZFP36L1*

To identify the upstream TF driving the SE-associated oncogene, the MEME-ChIP online tool was used to identify TF-binding sites in ZFP36L1-SE. Given the high GC content of E2, which is JQ1-insensitive, only the sequence motifs enriched in E1 (motif ID: GRGGMAGGARG) were examined. **Figure 4A** lists the predicted TFs and corresponding DNA motifs, including ETS transcription factor family (such as SPI1, ELF1 and ETS1) and E2F transcription factor family (such as E2F1 and E2F6). SPI1, ELF1, and E2F1 were confirmed using another online analysis tool based on ChIP-seq data from the Signaling Pathways Project**.** Among these, SPI1 is a known interferon regulatory TF that modulates PD-L1 mRNA expression [15]. Moreover, querying TCGA data revealed an association between SPI1 expression and poor prognosis **(Figure 4B**). Consequently, we speculated that SPI1 is a tissue-specific TF driving ZFP36L1 transcription by activating the SE region.

To validate this hypothesis, MKN45 cells were transfected with *SPI1*, *ELF1*, *E2F1*, and control plasmids. The RT-PCR results indicated that only transfection with SPI1 upregulated the *ZFP36L1* mRNA level **(Figure 4C)**. Similarly, *SPI1* overexpression increased the ZFP36L1 protein levels in MKN45 and MGC803 cells **(Figure 4D)**. TCGA data revealed that *SPI1* mRNA expression positively correlated with PD-L1 expression in patients with stomach cancer **(Figure 4E)**. Overexpression of *SPI1* increased IFN-γ-induced PD-L1 protein amount and fluorescent signal at membrane surfaces in GC cells, but concurrent knockdown of *ZFP36L1* could reverse the results of PD-L1 expression **(Figure 4F and Supplementary Figure 1F)**. These findings suggest that SPI1 regulates PD-L1 expression in a ZFP36L1-dependent manner.

Further analysis of protein-protein interaction networks using STRING indicated that SPI1 might interact with BRD4 and P300 proteins, which are SE-labeled molecules **(Figure 4G)**. Subsequently, the formation of the transcriptional complex comprising SPI1 and BRD4 was investigated. Exogenous BRD4 co-immunoprecipitated with exogenous SPI1 in 293T cells co-transfected with two plasmids, as observed using the anti-Flag affinity resin **(Figure 4H)**. In MGC803 cells, endogenous SPI1 immunoprecipitated with endogenous BRD4 **(Figure 4I)**. Additionally, we constructed a prokaryotic expression system of SPI1 and BRD4, and performed protein purification and GST pull-down assays **(Figure 4J)**. These results indicate that SPI1 and BRD4 directly bind in vitro, reflecting the specificity of SE-associated TFs.

To assess SE activity and TF occupancy, the E1 fragment was inserted into the luciferase reporter pGL4-Basic vector. In 293T cells, luciferase signals were enhanced when the *SPI1* plasmid, instead of *ELF1* or *E2F1*, was co-transfected with pGL4-E1 **(Figure 4K)**. This indicates a well-defined binding site for SPI1 in the ZFP36L1-E1 region, consistent with previous RT-PCR results.

The six predicted DNA sequence motifs in the E1 region are distributed among four DNA-binding sites, with sites C and D containing two adjacent DNA sequence motifs.

Subsequently, we performed ChIP experiments using SPI1 antibodies to immunoprecipitate bound DNA fragments in MGC803 cells, followed by RT-PCR analysis of the products. Among these endogenous SPI1 binding sites, the abundance of the site C product was the highest **(Figure 4L)**. Consequently, four truncated E1 fragments containing different binding sites were inserted into the luciferase reporter vector (E1A-E1D). As anticipated, we observed significantly enhanced luciferase activity upon co-transfection with the SPI1 and pGL4-E1C plasmids **(Figure 4M)**. Furthermore, two motifs totaling 15 bp were deleted from site C to construct a plasmid with a deletion mutation. The transcriptional activation of SPI1 was abrogated in the deletion mutation group compared with that in the wild-type group **(Figure 4N)**. These results suggest that site C is the SPI1 binding region in ZFP36L1-SE.

Upregulation of PD-L1 mediated by *HDAC3* mRNA decay

To identify downstream target genes, the mRNA transcripts bound to ZFP36L1 were searched against the RNAct website. A bibliometric analysis via PubMed suggested that 51 gene transcripts may be associated with PD-L1 expression **(Figure 5A)**. Representative molecules were selected to perform preliminary verification, which revealed that *HDAC3* mRNA expression was significantly reduced in MGC803 cells overexpressing ZFP36L1 **(Figure 5B)**. Conversely, protein levels of HDAC3 increased in XGC-1 and MKN45 cells with *ZFP36L1* knockdown **(Figure 5C)**. HDAC3 reportedly represses PD-L1 transcription through histone deacetylation [16, 17]. Likewise, we observed that overexpression of *HDAC3* does not directly affect PD-L1 promoter activity **(Figure 5D)**, but inhibits PD-L1 transcription through histone H3K27 deacetylation in the promoter region **(Figure 5E, F)**. Additionally, histone H3K27 deacetylation is also detrimental to the transcriptional activity of ZFP36L1-E1. Therefore, we conducted rescue experiments involving *HDAC3* plasmid co-transfection. The PD-L1-inducing effects of IFN-γ were reinforced in cell lines overexpressing *ZFP36L1* **(Figures 5I, J)**. However, PD-L1 protein levels and surface fluorescent signals decreased when *HDAC3* was simultaneously overexpressed. Additionally, the effects of *SPI1* overexpression were rescued when *HDAC3* expression was concurrently restored in MGC803 and MKN45 cells **(Figures 5K, L)**. These findings suggest that SE-driven ZFP36L1 positively regulates PD-L1 expression by inhibiting HDAC3. The inhibition of HDAC3 additionally provide positive feedback to promote *ZFP36L1* transcription.

Actinomycin D was employed to assess the rate of *HDAC3* mRNA degradation. *ZFP36L1* knockdown in MKN45 cells led to an increased half-life of *HDAC3* mRNA post-actinomycin D treatment, indicating enhanced mRNA stability and suppression of mRNA decay. Conversely, *ZFP36L1* overexpression in MGC803 cells promoted mRNA degradation, impairing *HDAC3* mRNA stability **(Figure 5M)**. This observation suggests that ZFP36L1 influences *HDAC3* mRNA decay.

To further elucidate the mechanism of RNA-binding protein leading to mRNA deadenylation, we conducted a series of experiments. Initially, we validated the direct binding of ZFP36L1 protein to the 3′UTR region of *HDAC3* mRNA via RNA immunoprecipitation. Owing to the lack of highly potent ZFP36L1 antibodies, RNA fragments were enriched using an anti-FLAG antibody in MGC803 cells overexpressing exogenous FLAG-tagged ZFP36L1. While we observed no significant change in HPRT1 mRNA (negative control), the abundance of HDAC3 mRNA fragments was amplified in the immunoprecipitated products **(Figure 5N)**.

Subsequently, the binding site in the ARE of the 3′UTR was identified. Classical binding motifs of the ZFP36 protein family, such as "WTTTW" and "WWTTTWW," were considered. The 3′UTR sequences of *HDAC3* mRNA were examined, revealing that only "ATTTA" fulfilled the requirements. The 3′UTR sequences and pmirGLO vectors were used to introduce a point mutation into the luciferase reporter gene plasmid, where the central base sequence of "ATTTA" was substituted with "ACCCA." ZFP36L1 impaired the transcriptional activity of the wild-type plasmid but not the mutant plasmid, directly demonstrating the regulatory site of mRNA decay-promoting activity **(Figure 5O)**.

Finally, the CCCH-type zinc finger domains were examined to confirm their indispensable role in RNA binding. Accordingly, we mutated two cysteine (C) residues at positions 135 and 173 to arginine (R) **(Figure 5P)**. *HDAC3* mRNA probes were synthesized and co-incubated with extracts of MGC803 cells transfected with a mutant (C135R–C173R) or wild-type plasmid. RNA pull-down assay results revealed that the mutant ZFP36L1 did not bind to the 3′UTR of HDAC3 mRNA. Collectively, our findings suggest that ZFP36L1 potentiated PD-L1 expression by promoting *HDAC3* mRNA decay.

Correlation between ZFP36L1 and PD-L1 in vivo

Protein expression levels were assessed in 70 PD-L1 positive GC tumor tissues via IHC staining. The IHC score of ZFP36L1 positively correlated with PD-L1 and SPI1 while exhibiting a negative correlation with HDAC3 **(Figure 6A-C)**. These results substantiate the upstream-downstream relationship observed in human tissue specimens.

Wild-type mice with normal immune function were chosen to explore these regulatory relationships in vivo. The mouse GC cell line MFC was substituted with the MC38 cell line owing to its poor tumorigenic capacity in wild-type mice. Subsequently, stable knockdown mouse *ZFP36L1* (mZFP36L1) cell lines were established for subcutaneous tumor formation and tail vein assay of lung metastasis **(Figure 6D)**. Although mZFP36L1 knockdown did not impact the size of subcutaneous tumors **(Figure 6E)**, it led to reduced mRNA and protein expression of mPD-L1 **(Figure 6F, G)**. Furthermore, the mice in the mZFP36L1 knockdown group exhibited fewer metastatic pulmonary nodules compared with that in mice in the control group **(Figure 6H)**, with representative lung tissue sections demonstrating strong positivity for CD8α **(Figure 6I)**. Conversely, the number of pulmonary metastatic nodules was not decreased in the T-cell-deficient nude mice injected with mZFP36L1 knockdown cells **(Figure 6J)**. These findings suggest potential immunotherapeutic benefits associated with targeting ZFP36L1. **Figure 7** illustrates the SPI1–ZFP36L1–HDAC3–PD-L1 signaling axis, depicting the interconnected regulatory relationship among these molecules.

Discussion

In the present study, we identified the SE heterogeneity between two subtypes of GC with differential growth patterns. SEs have emerged as a whole novel branch within tumor epigenetics. The direct experimental validation of SEs involves assessing the expression of target genes after the deletion of SE regions via the CRISPR/Cas9 system. In the context of bladder cancer, FOSL1 directly binds to SNHG15-SE, stimulating the Wnt signaling pathway through interactions with SNHG15–CTNNB1, thereby driving malignant behavior [18]. Exploring different loci enables the identification of crucial SE peaks and their functional roles. For instance, *TOX2* acts as an SE-driven oncogene in extranodal natural killer/T-cell lymphoma, with its transcription governed by the SE-specific TFs, RUNX3. Targeting SE regions with various single-guide RNAs (sgRNAs) has

confirmed the pathogenicity of TOX2-SE [19]. While the CRISPR/Cas9 system was not directly investigated in this study, the biological mechanism underlying ZFP36L1-SE was indirectly corroborated using ChIP, BRD4 co-immunoprecipitation (CoIP), and luciferase assays. The interactions between promoters and SEs are reportedly mediated by CCCTC-binding factor (CTCF) loops. Recently, researchers have identified novel regulatory elements within SEs, termed "facilitators," which highlights the significance of SE integrity [20]. Furthermore, SEs can transcribe SE RNA (seRNA), which is beneficial for chromatin openness [21]. Collectively, further investigation into the functional architecture of SEs is warranted.

Understanding the mechanisms governing SE formation is currently a prominent area of research. *PDZK1IP1* is an acquired SE-driven oncogene in primary colorectal tumors, with its encoded protein regulating the pentose phosphate pathway to promote tumor redox capability. Although PDZK1IP1–SE does not initially exist in colon cancer cell lines, its production is stimulated by abundant inflammatory factors within the tumor microenvironment [22]. These acquired somatic mutations exert influence over transcriptional epigenetic regulation. Acquired SEs in GC exhibit a high binding affinity for CDX2 or HNF4α, alongside enriched chromatin interactions and cancer-associated single nucleotide polymorphisms (SNPs) [23]. Liu et al. identified a genetic variation (SNP rs10470352) within the SOX2-SE region through a joint analysis of genome-wide association studies (GWAS) and HiChIP. This sequence variation enables TP73/RUNX3 occupancy, promoting active chromatin and upregulating *SOX2* expression [24]. However, the infiltration-specific nature of ZFP36L1-SE raises questions regarding whether its pro-tumor function is attributable to somatic mutations.

We demonstrate for the first time that ZFP36L1 driven by ZFP36L1-SE promotes IFN-γ-induced PD-L1 expression. Given that the mRNA of numerous inflammatory factors and oncogenes harbor AREs in their 3′UTR, ZFP36 family proteins are typically regarded as anti-tumor and anti-inflammatory agents. Loh et al. proposed that *ZFP36L1* deletion mutations are characteristic of urological tumors owing to their targeting of hypoxic mRNAs or cell cycle markers, such as *HIF1A*, *CCND1*, and *E2F1*, thereby promoting their degradation [25]. The authors also reported the inhibition of the HDAC family by ZFP36L1. In small-cell lung cancer, inhibition of lysine-specific demethylase 1 (LSD1) triggers *ZFP36L1* expression, leading to the decay of *SOX2* mRNA and attenuation of tumor neuroendocrine differentiation [26]. This highlights the complex role of ZFP36L1, thereby cautioning about simple dichotomy.

Novel treatment regimen in combination with anti-PD-L1 mainly enhanced CD8+ T-cell infiltration [27, 28]. Several studies have proposed that reducing PD-L1 expression enhances the tumor-killing effect of cytotoxic T lymphocytes in vitro and reduces primary tumor foci in vivo. Conversely, findings from this study suggest that PD-L1 expression is associated with immune evasion in metastatic foci [29]. The upstream regulation of PD-L1 expression occurs at both mRNA and protein levels. The well-established JAK-STAT/IRF1 signaling pathway primarily governs IFN-γ-induced PD-L1 transcription, with certain oncogenes such as *DENR*, *UBR5*, and *SOX10* promoting tumor immune evasion via activation of this pathway [17, 30, 31]. Additionally, CD274-associated transcriptional regulators include *HIF-1α*, *cMYC*, and *YBX1* [32]. Shang et al. demonstrated that MTHFD2 facilitates O-GlcNAc glycosylation of the c-MYC protein during metabolic reprogramming, thereby activating PD-L1 transcription [33]. However, ZFP36L1 disrupts *HDAC3* mRNA, leading to PD-L1-mediated immune evasion independent of the aforementioned TFs. It destabilizes the regulatory region of *CD274*, enhances histone acetylation, and promotes chromatin accessibility. Likewise, depletion of *ZNF652* disrupts the formation of the HDAC1/2-MTA3 co-repressor complex, resulting in elevated PD-L1 expression in triple-negative breast cancer [34].

Conversely, the m6A reader IGF2BP1 binds to the 3′UTR, initiating m6A modification and stabilizing PD-L1 mRNA [35].

The regulatory mechanisms governing PD-L1 predominantly involve post-translational modifications and subcellular relocalization. K48-linked deubiquitination by USP2 and N-glycosylation by B4GALT1 stabilize PD-L1 and prevent its degradation. Both K48-linked de-ubiquitination by USP2 and N-glycosylation by B4GALT1 are able to stabilize and prevent degradation of PD-L1 protein [36, 37]. TRIM28 overexpression in GC reportedly prevents proteasomal degradation of PD-L1 protein through SUMOylation, as well as promotes PD-L1 transcription by activating the mTOR and TBK1–IRF1 pathways [38]. However, ZFP36L1 primarily exerts a negative influence on signaling pathways and is not associated with protein modification. In terms of subcellular relocalization, the mitochondrial membrane protein ATAD3A in paclitaxel-resistant breast cancer patients obstructs the mitochondrial translocation and autophagic degradation of PD-L1, resulting in increased membranous PD-L1 expression [39]. ZFP36L1 reportedly forms a subcellular compartment with the endoplasmic reticulum (ER), facilitating the formation of membrane-less organelles in the TIS11B (ZFP36L1) granule ER domain. Within this domain, the interaction between SET and CD47/CD274, which harbor multiple AREs, promotes membrane protein expression [40]; follow-up studies are warranted to comprehensively elucidate its role.

In conclusion, our findings elucidate the regulation of the SPI1–ZFP36L1–HDAC3–PD-L1 axis in infiltrative GC and highlight immune escape signatures driven by SEs. These findings offer complementary insights for the application of immunotherapy in GC.

Abbreviations

3′UTR: 3′ untranslated region; ARE: adenylate uridylate rich element; CTCF: CCCTC-binding factor; ER: endoplasmic reticulum; GC: gastric cancer; GO–KEGG: Gene Ontology- Kyoto Encyclopedia of Genes and Genomes; HDAC3: Histone deacetylase 3; IHC: immunohistochemistry; PD-L1: programmed cell death-ligand-1; ROSE: ranking of SE; SE: Super-enhancers; SNPs: single nucleotide polymorphisms; TCGA: The Cancer Genome Atlas; TIDE: Tumor Immune Dysfunction and Exclusion; TSS: Transcription Start Site; TTS: Transcription Termination Site; ZFP36L1: zinc finger protein 36.

Conflict of Interest

The authors declare that the research was conducted in the absence of any commercial or financial relationships that could be construed as a potential conflict of interest.

Author Contributions

Jianchun Cai: obtained funding and designed the project. Huiqin Zhuo: obtained funding, organized and supervised the study. Xujin Wei: carried out the experiments and drafted the manuscript. Jie Liu: data analysis and writing of manuscript. Wangyu Cai, Jia Cheng, and Wen Xie: validated the data and provided conceptual advice. Kang Wang, Lingyun Lin, and Jingjing Hou: technical and material support.

Funding

This work was supported by National Natural Science Foundation of China (No. 81871979, No. 82272894); Natural Science Foundation of Fujian Province (No. 2021J02056, No. 2020CXB048, No. 2021D026 and No. 2023J011594); the Medical and Health Sciences Foundation of Xiamen (Nos. 3502Z20199171 and 3502Z20204002); Xiamen Medical and Health Guidance Project (No. 3502Z20214ZD1038); and Science and Technology Planning Project of Fujian Provincial Health Commission (No. 2020GGB056).

Acknowledgments

We thank Xin Chen, Hao Zhang, Shihao Rao, and Cheng Huang for the experimental assistance.

Data Availability Statement

TCGA data were downloaded from the UCSC Xena website http://xena.ucsc.edu/ ; RNA-binding protein prediction website: http://rnact.crg.eu ; ChIP-seq prediction of transcription factors: https://www.signalingpathways.org.

Ethics Statement

The study was conducted in accordance with the Declara-tion of Helsinki. The Ethics Committee of Zhongshan Hospital of Xiamen University reviewed and approved this study: xmzsyyky-2020-126, 3 September, 2020. The number of animal experiments ethical approval is XMULAC20220268.

References

1. Qi J, Li M, Wang L, Hu Y, Liu W, Long Z, et al. National and subnational trends in cancer burden in China, 2005–20: an analysis of national mortality surveillance data. The Lancet Public Health. 2023;8(12):e943-e55.

2. Ming S. Gastric carcinoma. A pathobiological classification. Cancer. 1977;39(6):2475-85.

3. Guan WL, He Y, Xu RH. Gastric cancer treatment: recent progress and future perspectives. J Hematol Oncol. 2023;16(1):57.

4. Janjigian YY, Kawazoe A, Bai Y, Xu J, Lonardi S, Metges JP, et al. Pembrolizumab plus trastuzumab and chemotherapy for HER2-positive gastric or gastro-oesophageal junction adenocarcinoma: interim analyses from the phase 3 KEYNOTE-811 randomised placebo-controlled trial. The Lancet. 2023.

5. Whyte WA, Orlando DA, Hnisz D, Abraham BJ, Lin CY, Kagey MH, et al. Master transcription factors and mediator establish super-enhancers at key cell identity genes. Cell. 2013;153(2):307-19.

6. Liu Z, Ye Y, Liu Y, Liu Y, Chen H, Shen M, et al. RNA Helicase DHX37 Facilitates Liver Cancer Progression by Cooperating with PLRG1 to Drive Superenhancer-Mediated Transcription of Cyclin D1. Cancer Research. 2022;82(10):1937-52.

7. Berico P, Nogaret M, Cigrang M, Lallement A, Vand-Rajabpour F, Flores-Yanke A, et al. Super-enhancer-driven expression of BAHCC1 promotes melanoma cell proliferation and genome stability. Cell Rep. 2023;42(11):113363.

8. Ye J, Cai S, Feng Y, Li J, Cai Z, Deng Y, et al. Metformin escape in prostate cancer by activating the PTGR1 transcriptional program through a novel super-enhancer. Signal Transduct Target Ther. 2023;8(1):303.

9. Ho S, Sheng T, Xing M, Ooi W, Xu C, Sundar R, et al. Regulatory enhancer profiling of mesenchymal-type gastric cancer reveals subtype-specific epigenomic landscapes and targetable vulnerabilities. Gut. 2023;72(2):226-41.

10. Snyder BL, Blackshear PJ. Clinical implications of tristetraprolin (TTP) modulation in the treatment of inflammatory diseases. Pharmacology & Therapeutics. 2022;239:108198.

11. Xing R, Zhou Y, Yu J, Yu Y, Nie Y, Luo W, et al. Whole-genome sequencing reveals novel tandem-duplication hotspots and a prognostic mutational signature in gastric cancer. Nature Communications. 2019;10(1):2037.

12. Hong Z, Xie W, Zhuo H, Wei X, Wang K, Cheng J, et al. Crosstalk between Cancer Cells and Cancer-Associated Fibroblasts Mediated by TGF-β1–IGFBP7 Signaling Promotes the Progression of Infiltrative Gastric Cancer. Cancers. 2023;15(15):3965.

13. Xu H, Peng J, Zhuang Y, Chen J, Luo Q, Huang W, et al. Establishment and characterization of an expanding-type gastric cancer cell line by Ming's classification. Oncology reports. 2016;36(5):3030-6.

14. Peng J, Xu H, Cai J. Establishment and characterization of a new gastric cancer cell line, XGC-1. Cancer Cell Intenational. 2020;20:437.

15. Li Q, Zhang L, You W, Xu J, Dai J, Hua D, et al. PRDM1/BLIMP1 induces cancer immune evasion by modulating the USP22-SPI1-PD-L1 axis in hepatocellular carcinoma cells. Nature Communications. 2022;13(1).

16. Wang H, Fu C, Du J, Wang H, He R, Yin X, et al. Enhanced histone H3 acetylation of the PD-L1 promoter via the COP1/c-Jun/HDAC3 axis is required for PD-L1 expression in drug-resistant cancer cells. Journal of Experimental & Clinical Cancer Research. 2020;39(1).

17. Yokoyama S, Takahashi A, Kikuchi R, Nishibu S, Lo JA, Hejna M, et al. SOX10 Regulates Melanoma Immunogenicity through an IRF4–IRF1 Axis. Cancer Research. 2021;81(24):6131-41.

18. Tan M, Pan Q, Gong H, Zhai X, Wan Z, Ge M, et al. Super-enhancer-associated SNHG15 cooperating with FOSL1 contributes to bladder cancer progression through the WNT pathway. Pharmacol Res. 2023;197:106940.

19. Zhou J, Toh SH, Tan TK, Balan K, Lim JQ, Tan TZ, et al. Super-enhancer-driven TOX2 mediates oncogenesis in Natural Killer/T Cell Lymphoma. Mol Cancer. 2023;22(1):69.

20. Blayney JW, Francis H, Rampasekova A, Camellato B, Mitchell L, Stolper R, et al. Super-enhancers include classical enhancers and facilitators to fully activate gene expression. Cell. 2023;186(26):5826-39.e18.

21. Li R, Zhao H, Huang X, Zhang J, Bai R, Zhuang L, et al. Super-enhancer RNA m6A promotes local chromatin accessibility and oncogene transcription in pancreatic ductal adenocarcinoma. Nature Genetics. 2023;55(12):2224-34.

22. Zhou RW, Xu J, Martin TC, Zachem AL, He J, Ozturk S, et al. A local tumor microenvironment acquired super-enhancer induces an oncogenic driver in colorectal carcinoma. Nature Communications. 2022;13(1).

23. Ooi WF, Xing M, Xu C, Yao X, Ramlee MK, Lim MC, et al. Epigenomic profiling of primary gastric adenocarcinoma reveals super-enhancer heterogeneity. Nature Communications. 2016;7:12983.

24. Liu S-X, Wang C, Lin R-B, Ding W-Y, Roy G, Wang H-B, et al. Super-enhancer driven SOX2 promotes tumor formation by chromatin re-organization in nasopharyngeal carcinoma. eBioMedicine. 2023;98:104870.

25. Loh X-Y, Sun Q-Y, Ding L-W, Mayakonda A, Venkatachalam N, Yeo M-S, et al. RNA-Binding Protein ZFP36L1 Suppresses Hypoxia and Cell-Cycle Signaling. Cancer Research. 2020;80(2):219-33.

26. Chen H, Durmaz Y, Li Y, Sabet A, Vajdi A, Denize T, et al. Regulation of neuroendocrine plasticity by the RNA-binding protein ZFP36L1. Nature communications. 2022;13(1):4998.

27. Chen H, Zhao L, Fu K, Lin Q, Wen X, Jacobson O, et al. Integrin αvβ3-targeted radionuclide therapy combined with immune checkpoint blockade immunotherapy synergistically enhances anti-tumor efficacy. Theranostics. 2019;9(25):7948-60.

28. Feng Y, Ning X, Wang J, Wen Z, Cao F, You Q, et al. Mace-Like Plasmonic Au-Pd Heterostructures Boost Near-Infrared Photoimmunotherapy. Advanced Science. 2023;10(6).

29. Klement JD, Redd PS, Lu C, Merting AD, Poschel DB, Yang D, et al. Tumor PD-L1 engages myeloid PD-1 to suppress type I interferon to impair cytotoxic T lymphocyte recruitment. Cancer Cell. 2023;41(3):620-36 e9.

30. Chen B, Hu J, Hu X, Chen H, Bao R, Zhou Y, et al. DENR controls JAK2 translation to induce PD-L1 expression for tumor immune evasion. Nature Communications. 2022;13(1):2059.

31. Wu B, Song M, Dong Q, Xiang G, Li J, Ma X, et al. UBR5 promotes tumor immune evasion through enhancing IFN-gamma-induced PDL1 transcription in triple negative breast cancer. Theranostics. 2022;12(11):5086-102.

32. Ru J, Lu J, Ge J, Ding B, Su R, Jiang Y, et al. IRGM is a novel regulator of PD-L1 via promoting S6K1-mediated phosphorylation of YBX1 in hepatocellular carcinoma. Cancer Letters. 2023:216495.

33. Shang M, Yang H, Yang R, Chen T, Fu Y, Li Y, et al. The folate cycle enzyme MTHFD2 induces cancer immune evasion through PD-L1 up-regulation. Nature Communications. 2021;12(1):1940.

34. Liu Y, Peng Y, Du W, Yu C, Peng Z, Qin L, et al. PD-L1-mediated immune evasion in triple-negative breast cancer is linked to the loss of ZNF652. Cell Reports. 2023;42(11):113343.

35. Jiang T, Xia Y, Li Y, Lu C, Lin J, Shen Y, et al. TRIM29 promotes antitumor immunity through enhancing IGF2BP1 ubiquitination and subsequent PD-L1 downregulation in gastric cancer. Cancer Letters. 2024;581:216510.

36. Kuang Z, Liu X, Zhang N, Dong J, Sun C, Yin M, et al. USP2 promotes tumor immune evasion via deubiquitination and stabilization of PD-L1. Cell Death & Differentiation. 2023;30(10):2249-64.

37. Cui Y, Li J, Zhang P, Yin D, Wang Z, Dai J, et al. B4GALT1 promotes immune escape by regulating the expression of PD-L1 at multiple levels in lung adenocarcinoma. Journal of Experimental & Clinical Cancer Research. 2023;42(1).

38. Ma X, Jia S, Wang G, Liang M, Guo T, Du H, et al. TRIM28 promotes the escape of gastric cancer cells from immune surveillance by increasing PD-L1 abundance. Signal Transduction and Targeted Therapy. 2023;8(1).

39. Xie X-Q, Yang Y, Wang Q, Liu H-F, Fang X-Y, Li C-L, et al. Targeting ATAD3A-PINK1-mitophagy axis overcomes chemoimmunotherapy resistance by redirecting PD-L1 to mitochondria. Cell Research. 2023;33(3):215-28.

40. Ma W, Mayr C. A Membraneless Organelle Associated with the Endoplasmic Reticulum Enables 3′UTR-Mediated Protein-Protein Interactions. Cell. 2018;175(6):1492-506.e19.

Figure Legends

Figure 1. Immune escape signatures of Ming infiltrative gastric cancer (GC) driven by super-enhancers (SEs). **(A)** Hematoxylin-eosin staining of GC. **(B)** SE peaks of H3K27ac histone modifications. **(C)** Distribution of H3K27ac SE peaks. **(D)** Venn diagrams of SE-driven genes and chromosomal landscape of infiltrative SE-driven genes. **(E)** Gene Ontology-Kyoto Encyclopedia of Genes and Genomes (GO-KEGG) pathway enrichment for SE-driven genes. **(F)** Unsupervised hierarchical clustering using 16 prognostic genes. **(G)** Kaplan–Meier survival curves of two subgroups. **(H)** Immune infiltration analysis. **(I)** Immunohistochemical (IHC) scores of programmed death-ligand 1 (PD-L1) in 70 GC tissues. TSS, Transcription Start Site; TTS, Transcription Termination Site.

Figure 2. Expression levels of *ZFP36L1* in infiltrative GC driven by ZFP36L1-SE. **(A)** Friends analysis of 16 SE-driven prognostic genes. **(B)** Correlations between clinical characteristics and the *ZFP36L1* mRNA expression in TCGA. **(C)** Tumor Immune Dysfunction and Exclusion scores in high and low expression levels of *ZFP36L1* groups. **(D)** Correlation between immune infiltration cells and the mRNA expression level of *ZFP36L1* in TCGA. **(E)** Correlation between *ZFP36L1* mRNA expression and immune checkpoints in TCGA. **(F)** H3K27ac signals of SEs and target genes in infiltrative GC. **(G)** H3K27ac signals of ZFP36L1-SE in GC. **(H)** Protein expression of *ZFP36L1* in 12 tumor and paired adjacent normal tissues of patients with infiltrative GC. **(I)** Protein expression of *ZFP36L1* in six GC cell lines. **(J)** Expression level of *ZFP36L1* after SE inhibition treatment. **(K)** H3K27ac signals of ZFP36L1-SE after SE inhibition treatment.

Figure 3. ZFP36L1 promotes IFN-γ-induced PD-L1 expression. **(A)** mRNA and **(C)** protein expression of PD-L1 in GC cell lines with or without ZFP36L1 knockdown. **(B)** mRNA and **(D)** protein expression of PD-L1 in GC cell lines with or without ZFP36L1 overexpression. **(E)** Fluorescent signal of the PD-L1 membrane protein in GC cell lines with or without ZFP36L1 knockdown and **(F)** overexpression.

Figure 4. SPI1 binds to the ZFP36L1-SE region and drives the regulation of PD-L1. **(A)** Schematic of transcription factor motif enrichment in ZFP36L1-E1. **(B)** Kaplan–Meier survival plot of SPI1 in TCGA. **(C)** mRNA and **(D)** protein expression of ZFP36L1 after transcription factors (TFs) plasmid transfection. **(E)** Correlation between SPI1 and PD-L1 in TCGA. **(F)** PD-L1 protein expression in simultaneous SPI1 overexpression and ZFP36L1 knockdown cells. **(G)** Prediction of SPI1–BRD4–P300 binding on the STRING website. Co-immunoprecipitation between **(H)** exogenous SPI1 and BRD4 in 293T cells , or **(I)** endogenous SPI1 and BRD4 in MGC803. **(J)** SPI1 directly interacts with BRD4 in vitro by GST pull-down experiment. **(K)** ZFP36L1-E1 binding of different TFs detected using dual-luciferase assay. **(L)** SPI1 enriched regions in ZFP36L1-E1 detected using dual-luciferase

assay. **(M)** Different binding sites of SPI1 in ZFP36L1-E1 detected using dual-luciferase assay. **(N)** Wild-type and motif-deletion mutant E1C binding of SPI1 detected using dual-luciferase.

Figure 5. ZFP36L1 positively regulates PD-L1 by activating *HDAC3* mRNA decay. **(A)** Word cloud of predicted ZFP36L1 target genes. **(B)** The mRNA expression of predicted target genes in MGC803 cell overexpressing ZFP36L1. **(C)** HDAC3 protein expression in *ZFP36L1* knockdown cells. **(D)** Effect of HDAC3 on *CD274* promoter activity in 293T using dual-luciferase assay. **(E)** Correlation between changes of histone H3K27 acetylation and PD-L1 protein expression in MKN45 cells overexpressing *HDAC3*. **(F)** The histone H3K27 acetylation levels of *CD274* promoter regions using ChIP assay. **(G)** Correlation between changes of histone H3K27 acetylation and ZFP36L1 protein expression. **(H)** The H3K27ac and SPI1 enrichment of ZFP36L1-E1C regions using ChIP assay. **(I-J)** PD-L1 protein expression in simultaneous *ZFP36L1* and *HDAC3* overexpression cells. **(M)** *HDAC3* mRNA decay in *ZFP36L1* knockdown and overexpression cells after actinomycin D treatment. **(N)** ZFP36L1 mRNA-binding level by RNA-binding protein immunoprecipitation. **(O)** ZFP36L1 mRNA-binding site in AU-rich element (ARE) of 3′UTR confirmed using dual-luciferase assay. **(P)** CCCH-type zinc finger domain of ZFP36L1 protein binding to *HDAC3* mRNA confirmed using RNA pull-down assay. ARE, adenylate uridylate- (AU-) rich element; 3′UTR, 3′ untranslated region.

Figure 6. Positive correlation between ZFP36L1 and PD-L1 in vivo. **(A-C)** IHC staining of SPI1, ZFP36L1 and HDAC3 protein in 70 PD-L1-positive GC tumor tissues. **(D)** Schematic diagram of experiments in C57BL/6J and BALB/c-nu mice. **(E)** Subcutaneous tumor weight from mice injected with control and ZFP36L1 knockdown cells. **(F)** The PD-L1 mRNA expression in subcutaneous tumors. **(G)** IHC staining of ZFP36L1 and PD-L1 protein in subcutaneous tumors. **(H)** Number of pulmonary metastases in different groups of C57BL/6J mice after tail vein injection of control and *ZFP36L1* knockdown cells. **(I)** Hematoxylin & eosin (HE) and IHC staining of CD8α in pulmonary metastases. **(J)** Number of pulmonary metastases in different groups of BALB/c-nu mice after tail vein injection of control and *ZFP36L1* knockdown cells.

Figure 7. Schematic diagram of SPI1–ZFP36L1–HDAC3–PD-L1 signaling axis (created with gdp.renlab.cn).

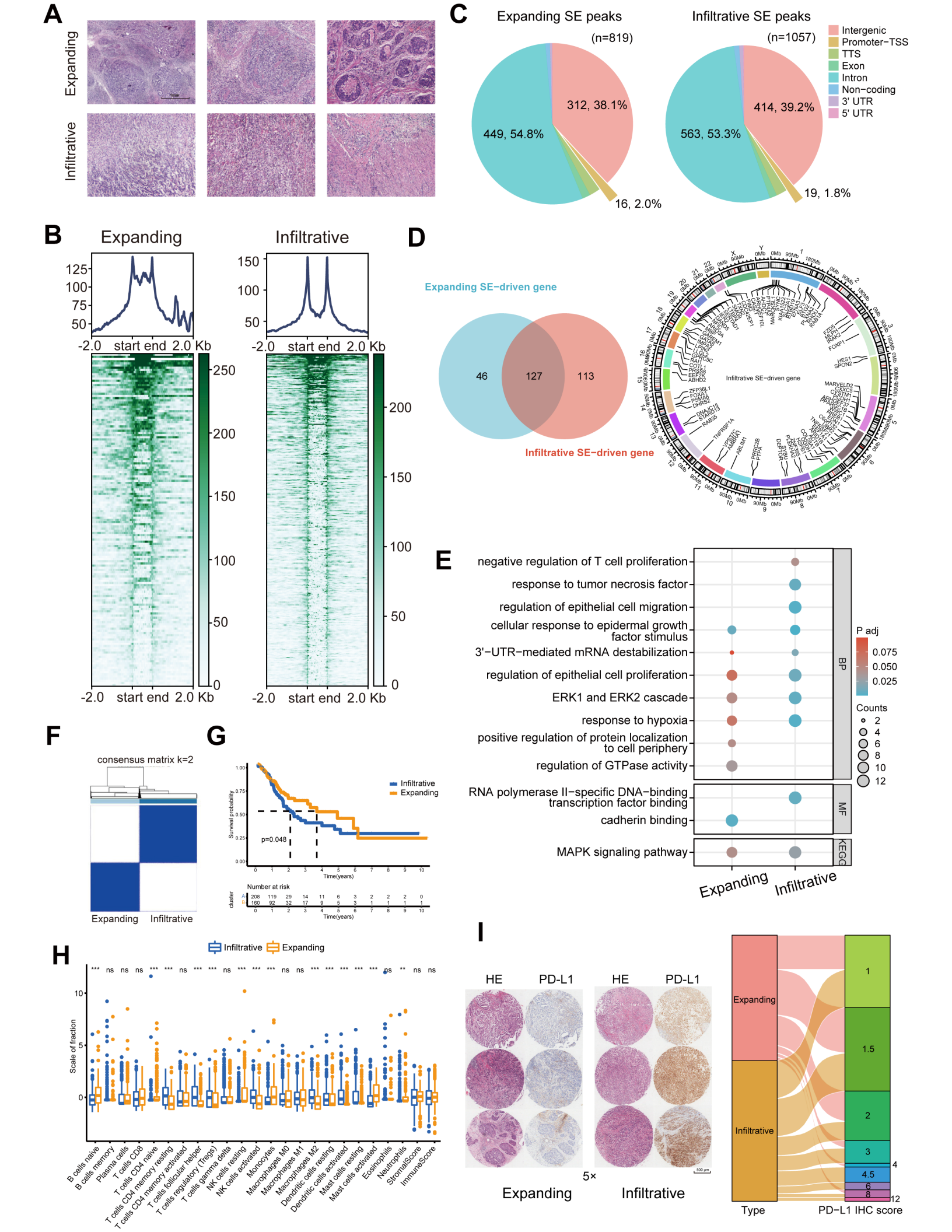
A
Expanding
Infiltrative
B
Expanding
Infiltrative
-2.0 start end 2.0 Kb
C
Expanding SE peaks
(n=819)
312, 38.1%
449, 54.8%
16, 2.0%
Infiltrative SE peaks
(n=1057)
414, 39.2%
563, 53.3%
19, 1.8%
Intergenic
Promoter-TSS
TTS
Exon
Intron
Non-coding
3' UTR
5' UTR
D
Expanding SE-driven gene
46
127
113
Infiltrative SE-driven gene
Infiltrative SE-driven gene
E
negative regulation of T cell proliferation
response to tumor necrosis factor
regulation of epithelial cell migration
cellular response to epidermal growth factor stimulus
3'-UTR-mediated mRNA destabilization
regulation of epithelial cell proliferation
ERK1 and ERK2 cascade
response to hypoxia
positive regulation of protein localization to cell periphery
regulation of GTPase activity
RNA polymerase II-specific DNA-binding transcription factor binding
cadherin binding
MAPK signaling pathway
BP
MF
KEGG
P adj
0.075
0.050
0.025
Counts
Expanding
Infiltrative
F
consensus matrix k=2
Expanding
Infiltrative
G
Infiltrative
Expanding
Survival probability
p=0.048
Time(years)
Number at risk
cluster
H
Infiltrative
Expanding
Scale of fraction
B cells naive
B cells memory
Plasma cells
T cells CD8
T cells CD4 naive
T cells CD4 memory resting
T cells CD4 memory activated
T cells follicular helper
T cells regulatory (Tregs)
T cells gamma delta
NK cells resting
NK cells activated
Monocytes
Macrophages M0
Macrophages M1
Macrophages M2
Dendritic cells resting
Dendritic cells activated
Mast cells resting
Mast cells activated
Eosinophils
Neutrophils
StromalScore
ImmuneScore
I
HE
PD-L1
HE
PD-L1
5×
Expanding
Infiltrative
Expanding
Infiltrative
Type
PD-L1 IHC score

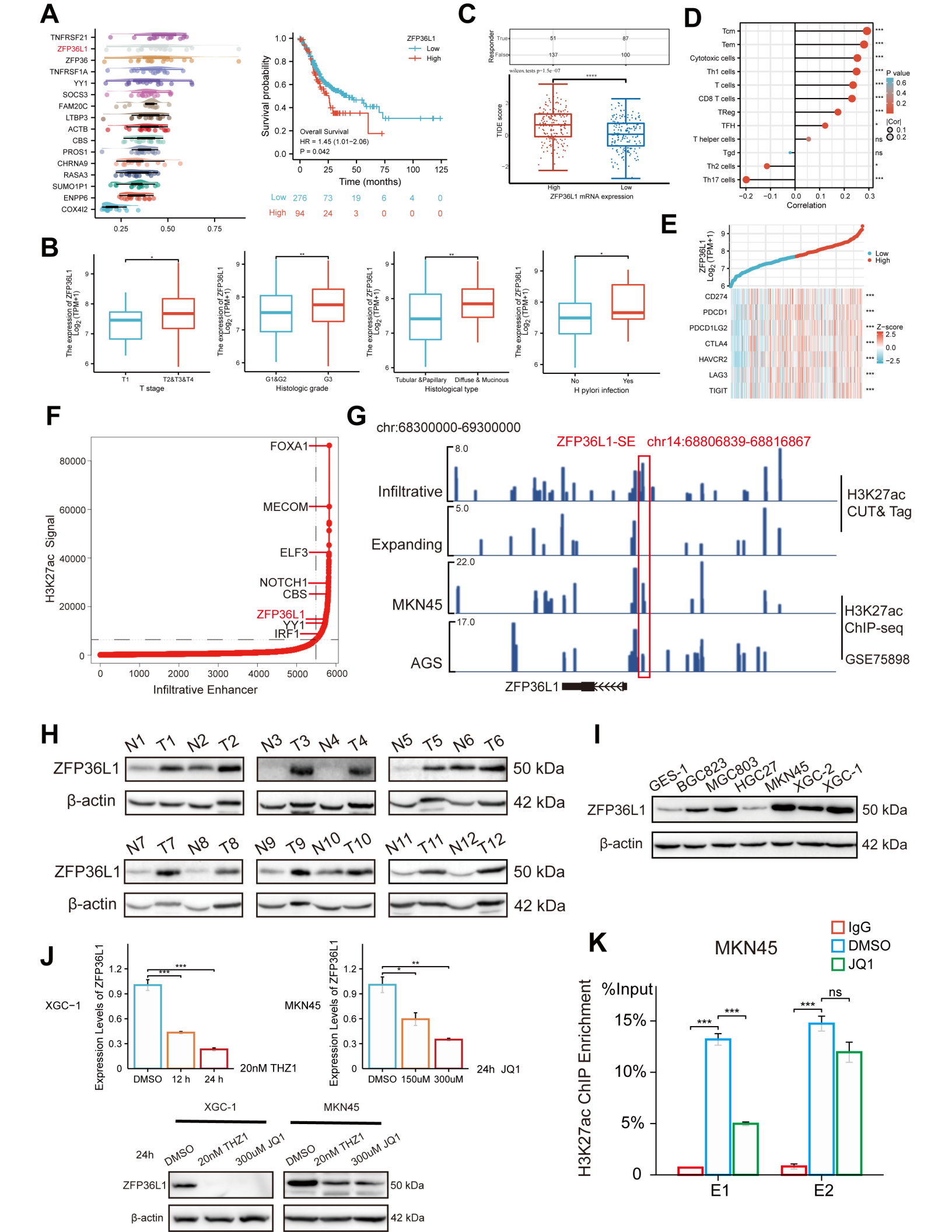
A
TNFRSF21
ZFP36L1
ZFP36
TNFRSF1A
YY1
SOCS3
FAM20C
LTBP3
ACTB
CBS
PROS1
CHRNA9
RASA3
SUMO1P1
ENPP6
COX4I2
0.25
0.50
0.75
Survival probability
ZFP36L1
Low
High
Overall Survival
HR = 1.45 (1.01−2.06)
P = 0.042
Time (months)
Low 276 73 19 6 4 0
High 94 24 3 0 0 0
C
Responder
True 51 87
False 137 100
wilcox.tests p=1.5e−07
TIDE score
High
Low
ZFP36L1 mRNA expression
D
Tcm
Tem
Cytotoxic cells
Th1 cells
T cells
CD8 T cells
TReg
TFH
T helper cells
Tgd
Th2 cells
Th17 cells
P value
|Cor|
Correlation
B
The expression of ZFP36L1 Log2 (TPM+1)
T1
T2&T3&T4
T stage
G1&G2
G3
Histologic grade
Tubular &Papillary
Diffuse & Mucinous
Histological type
No
Yes
H pylori infection
E
ZFP36L1 Log2 (TPM+1)
Low
High
CD274
PDCD1
PDCD1LG2
CTLA4
HAVCR2
LAG3
TIGIT
Z-score
F
H3K27ac Signal
FOXA1
MECOM
ELF3
NOTCH1
CBS
ZFP36L1
YY1
IRF1
Infiltrative Enhancer
G
chr:68300000-69300000
ZFP36L1-SE chr14:68806839-68816867
Infiltrative
Expanding
MKN45
AGS
H3K27ac CUT& Tag
H3K27ac ChIP-seq
GSE75898
ZFP36L1
H
N1 T1 N2 T2 N3 T3 N4 T4 N5 T5 N6 T6
ZFP36L1
β-actin
50 kDa
42 kDa
N7 T7 N8 T8 N9 T9 N10 T10 N11 T11 N12 T12
I
GES-1
BGC823
MGC803
HGC27
MKN45
XGC-2
XGC-1
ZFP36L1
β-actin
50 kDa
42 kDa
J
XGC−1
Expression Levels of ZFP36L1
DMSO
12 h
24 h
20nM THZ1
MKN45
DMSO
150uM
300uM
24h JQ1
XGC-1
MKN45
24h
DMSO
20nM THZ1
300uM JQ1
ZFP36L1
β-actin
50 kDa
42 kDa
K
MKN45
IgG
DMSO
JQ1
%Input
H3K27ac ChIP Enrichment
15%
10%
5%
0
E1
E2
ns

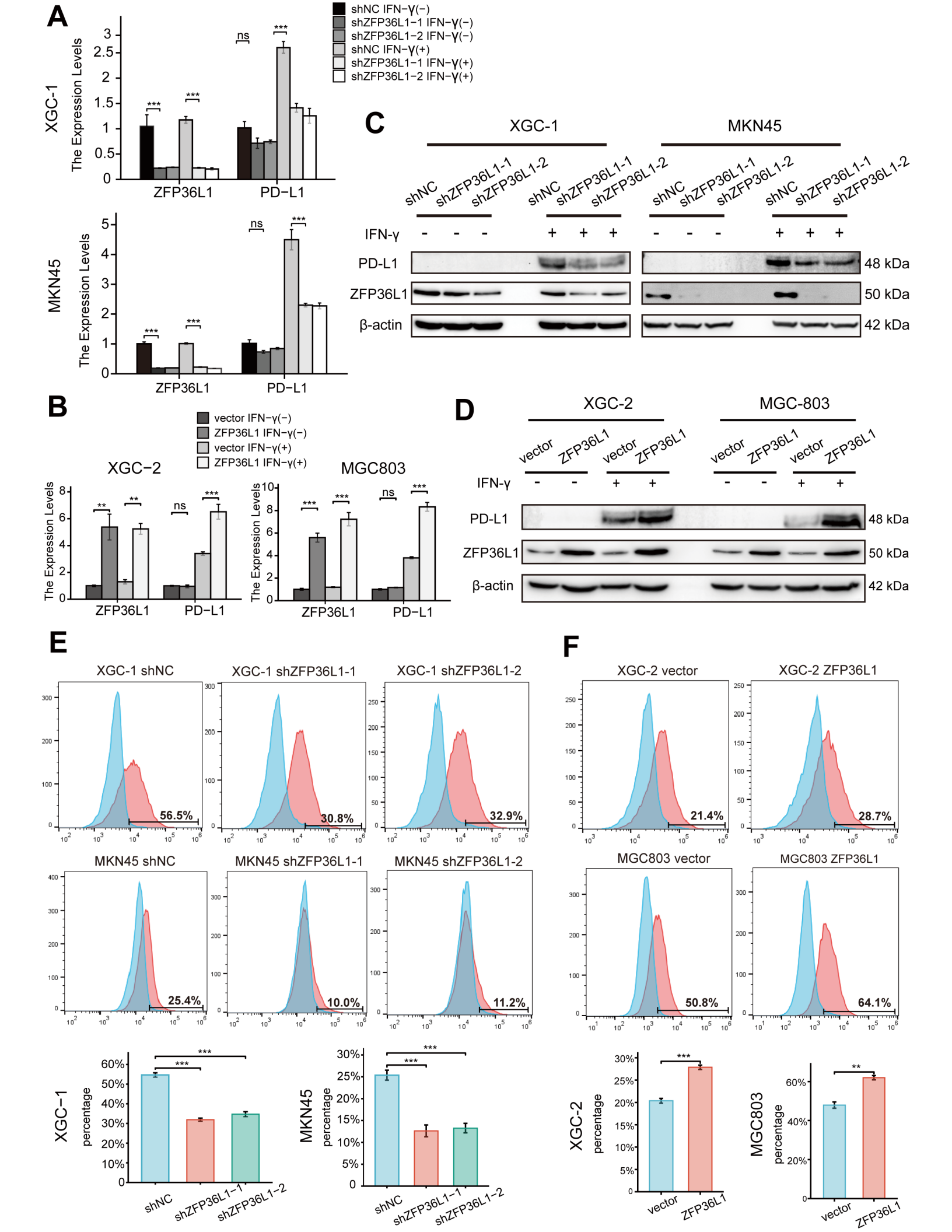
A
shNC IFN-γ(−)
shZFP36L1-1 IFN-γ(−)
shZFP36L1-2 IFN-γ(−)
shNC IFN-γ(+)
shZFP36L1-1 IFN-γ(+)
shZFP36L1-2 IFN-γ(+)
XGC-1
MKN45
The Expression Levels
ZFP36L1
PD-L1
ns
***
B
vector IFN-γ(−)
ZFP36L1 IFN-γ(−)
vector IFN-γ(+)
ZFP36L1 IFN-γ(+)
XGC-2
MGC803
**
C
XGC-1
MKN45
shNC
shZFP36L1-1
shZFP36L1-2
IFN-γ
PD-L1
ZFP36L1
β-actin
48 kDa
50 kDa
42 kDa
D
XGC-2
MGC-803
vector
ZFP36L1
E
XGC-1 shNC
XGC-1 shZFP36L1-1
XGC-1 shZFP36L1-2
56.5%
30.8%
32.9%
MKN45 shNC
MKN45 shZFP36L1-1
MKN45 shZFP36L1-2
25.4%
10.0%
11.2%
percentage
F
XGC-2 vector
XGC-2 ZFP36L1
21.4%
28.7%
MGC803 vector
MGC803 ZFP36L1
50.8%
64.1%

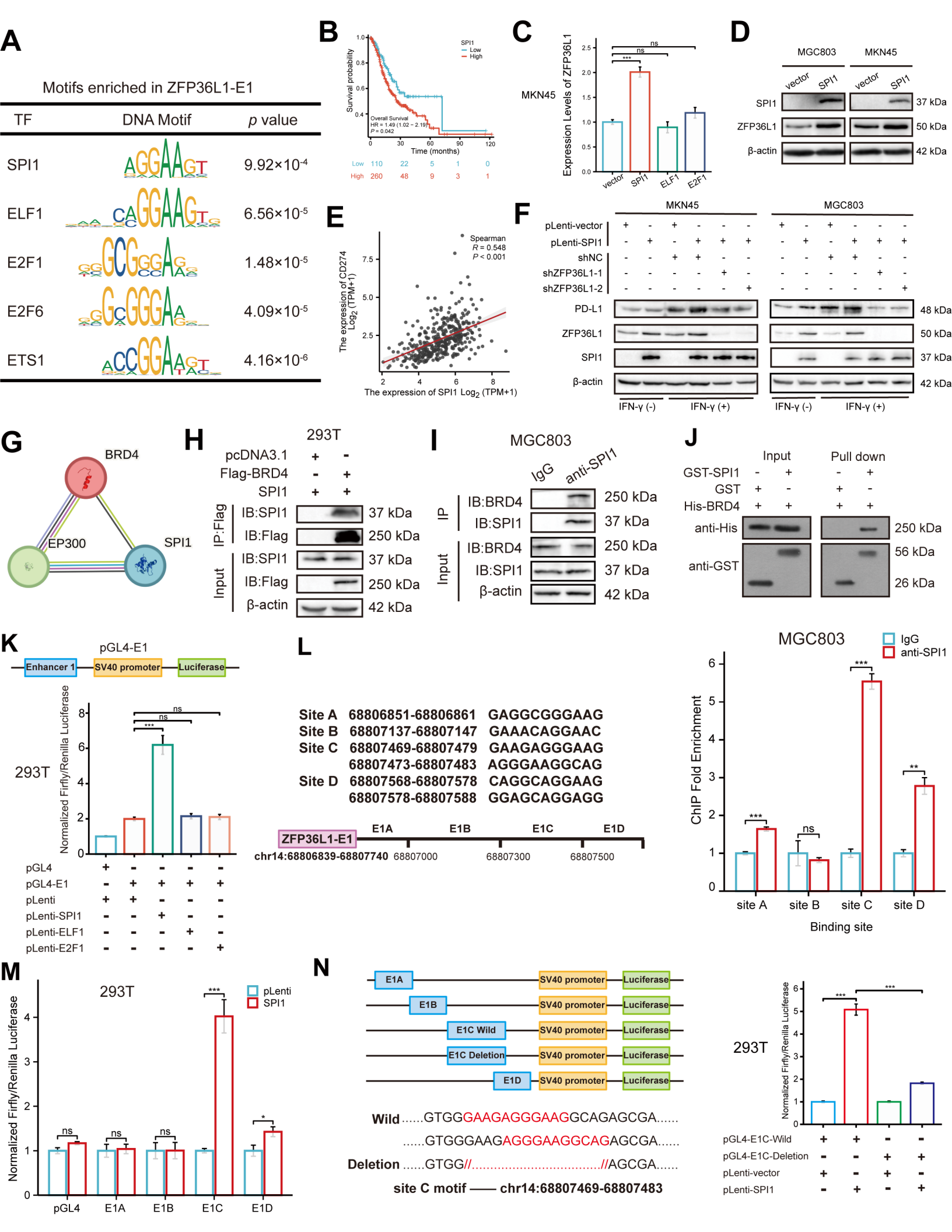
A
Motifs enriched in ZFP36L1-E1
TF
DNA Motif
p value
SPI1
9.92×10-4
ELF1
6.56×10-5
E2F1
1.48×10-5
E2F6
4.09×10-5
ETS1
4.16×10-6
B
Survival probability
SPI1
Low
High
Overall Survival
HR = 1.49 (1.02 – 2.19)
P = 0.042
Time (months)
Low 110 22 5 1 0
High 260 48 9 3 1
C
MKN45
Expression Levels of ZFP36L1
ns
***
vector
SPI1
ELF1
E2F1
D
MGC803
MKN45
vector
SPI1
SPI1
ZFP36L1
β-actin
37 kDa
50 kDa
42 kDa
E
Spearman
R = 0.548
P < 0.001
The expression of CD274 Log2 (TPM+1)
The expression of SPI1 Log2 (TPM+1)
F
MKN45
MGC803
pLenti-vector
pLenti-SPI1
shNC
shZFP36L1-1
shZFP36L1-2
PD-L1
ZFP36L1
SPI1
β-actin
48 kDa
50 kDa
37 kDa
42 kDa
IFN-γ (-)
IFN-γ (+)
G
BRD4
EP300
SPI1
H
293T
pcDNA3.1
Flag-BRD4
SPI1
IP:Flag
IB:SPI1
IB:Flag
Input
IB:SPI1
IB:Flag
β-actin
37 kDa
250 kDa
37 kDa
250 kDa
42 kDa
I
MGC803
IgG
anti-SPI1
IP
IB:BRD4
IB:SPI1
Input
IB:BRD4
IB:SPI1
β-actin
250 kDa
37 kDa
250 kDa
37 kDa
42 kDa
J
Input
Pull down
GST-SPI1
GST
His-BRD4
anti-His
anti-GST
250 kDa
56 kDa
26 kDa
K
pGL4-E1
Enhancer 1
SV40 promoter
Luciferase
293T
Normalized Firfly/Renilla Luciferase
ns
***
pGL4
pGL4-E1
pLenti
pLenti-SPI1
pLenti-ELF1
pLenti-E2F1
L
Site A 68806851-68806861 GAGGCGGGAAG
Site B 68807137-68807147 GAAACAGGAAC
Site C 68807469-68807479 GAAGAGGGAAG
68807473-68807483 AGGGAAGGCAG
Site D 68807568-68807578 CAGGCAGGAAG
68807578-68807588 GGAGCAGGAGG
ZFP36L1-E1
E1A
E1B
E1C
E1D
chr14:68806839-68807740
68807000
68807300
68807500
MGC803
IgG
anti-SPI1
ChIP Fold Enrichment
***
ns
**
site A
site B
site C
site D
Binding site
M
293T
pLenti
SPI1
Normalized Firfly/Renilla Luciferase
ns
*
***
pGL4
E1A
E1B
E1C
E1D
N
E1A
E1B
E1C Wild
E1C Deletion
E1D
SV40 promoter
Luciferase
Wild .....GTGGGAAGAGGGAAGGCAGAGCGA.....
.....GTGGGAAGAGGGAAGGCAGAGCGA.....
Deletion .....GTGG//.....//AGCGA.....
site C motif —— chr14:68807469-68807483
293T
Normalized Firfly/Renilla Luciferase
***
pGL4-E1C-Wild
pGL4-E1C-Deletion
pLenti-vector
pLenti-SPI1

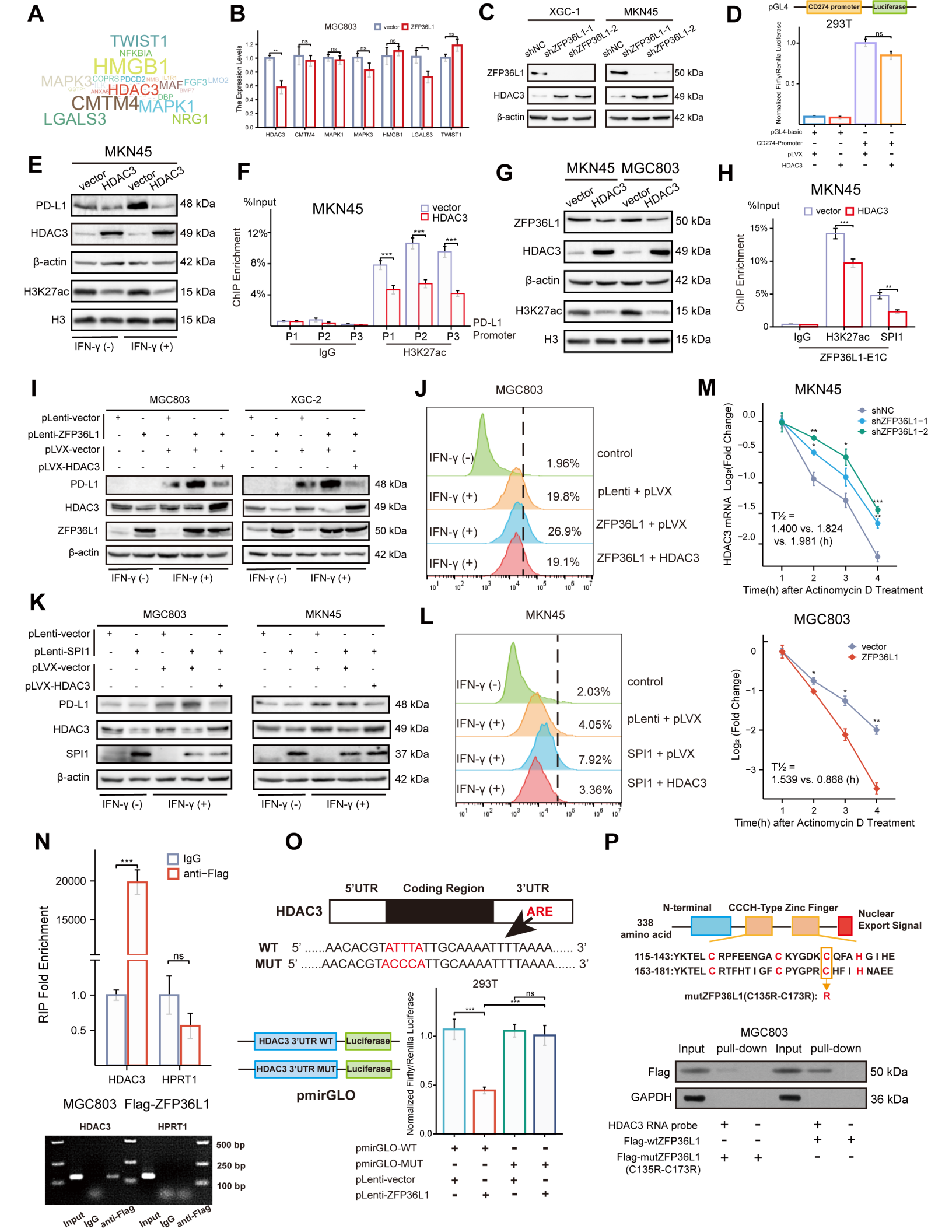
A
TWIST1
NFKBIA
HMGB1
MAPK3
COPRS
PDCD2
IL1R1
FGF3
LMO2
HDAC3
MAF
CMTM4
MAPK1
DBP
LGALS3
NRG1
B
MGC803
vector
ZFP36L1
The Expression Levels
HDAC3
CMTM4
MAPK1
MAPK3
HMGB1
LGALS3
TWIST1
C
XGC-1
MKN45
shNC
shZFP36L1-1
shZFP36L1-2
ZFP36L1
HDAC3
β-actin
50 kDa
49 kDa
42 kDa
D
pGL4
CD274 promoter
Luciferase
293T
Normalized Firfly/Renilla Luciferase
pGL4-basic
CD274-Promoter
pLVX
HDAC3
E
MKN45
vector
HDAC3
PD-L1
HDAC3
β-actin
H3K27ac
H3
48 kDa
49 kDa
42 kDa
15 kDa
15 kDa
IFN-γ (-)
IFN-γ (+)
F
%Input
MKN45
vector
HDAC3
ChIP Enrichment
12%
8%
4%
P1
P2
P3
IgG
H3K27ac
PD-L1 Promoter
G
MKN45
MGC803
vector
HDAC3
ZFP36L1
HDAC3
β-actin
H3K27ac
H3
50 kDa
49 kDa
42 kDa
15 kDa
15 kDa
H
MKN45
%Input
vector
HDAC3
ChIP Enrichment
15%
10%
5%
0
IgG
H3K27ac
SPI1
ZFP36L1-E1C
I
MGC803
XGC-2
pLenti-vector
pLenti-ZFP36L1
pLVX-vector
pLVX-HDAC3
PD-L1
HDAC3
ZFP36L1
β-actin
48 kDa
49 kDa
50 kDa
42 kDa
IFN-γ (-)
IFN-γ (+)
J
MGC803
IFN-γ (-)
1.96%
control
IFN-γ (+)
19.8%
pLenti + pLVX
IFN-γ (+)
26.9%
ZFP36L1 + pLVX
IFN-γ (+)
19.1%
ZFP36L1 + HDAC3
M
MKN45
shNC
shZFP36L1-1
shZFP36L1-2
HDAC3 mRNA Log₂(Fold Change)
T½ =
1.400 vs. 1.824
vs. 1.981 (h)
Time(h) after Actinomycin D Treatment
K
MGC803
MKN45
pLenti-vector
pLenti-SPI1
pLVX-vector
pLVX-HDAC3
PD-L1
HDAC3
SPI1
β-actin
48 kDa
49 kDa
37 kDa
42 kDa
IFN-γ (-)
IFN-γ (+)
L
MKN45
IFN-γ (-)
2.03%
control
IFN-γ (+)
4.05%
pLenti + pLVX
IFN-γ (+)
7.92%
SPI1 + pLVX
IFN-γ (+)
3.36%
SPI1 + HDAC3
MGC803
vector
ZFP36L1
Log₂ (Fold Change)
T½ =
1.539 vs. 0.868 (h)
Time(h) after Actinomycin D Treatment
N
IgG
anti-Flag
RIP Fold Enrichment
20000
15000
1.0
0.5
HDAC3
HPRT1
MGC803 Flag-ZFP36L1
HDAC3
HPRT1
500 bp
250 bp
100 bp
Input
IgG
anti-Flag
O
5'UTR
Coding Region
3'UTR
HDAC3
ARE
WT 5' .....AACACGTATTTATTGCAAAATTTTAAAA..... 3'
MUT 5' .....AACACGTACCCATTGCAAAATTTTAAAA..... 3'
HDAC3 3'UTR WT
Luciferase
HDAC3 3'UTR MUT
Luciferase
pmirGLO
293T
Normalized Firfly/Renilla Luciferase
pmirGLO-WT
pmirGLO-MUT
pLenti-vector
pLenti-ZFP36L1
P
N-terminal
CCCH-Type Zinc Finger
Nuclear Export Signal
338 amino acid
115-143:YKTEL C RPFEENGA C KYGDK C QFA H G I HE
153-181:YKTEL C RTFHT I GF C PYGPR C HF I H NAEE
mutZFP36L1(C135R-C173R): R
MGC803
Input
pull-down
Input
pull-down
Flag
GAPDH
50 kDa
36 kDa
HDAC3 RNA probe
Flag-wtZFP36L1
Flag-mutZFP36L1 (C135R-C173R)

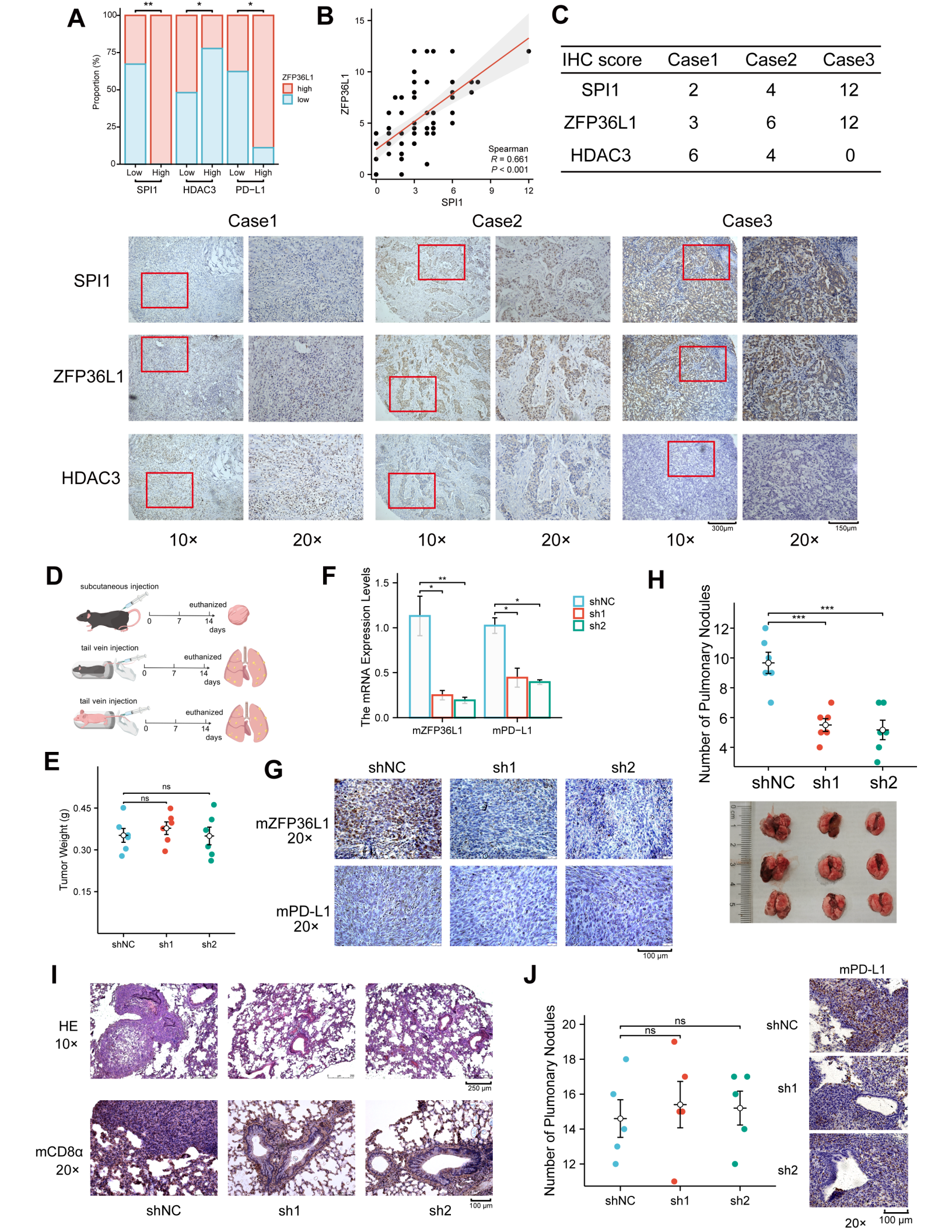

IHC score	Case1	Case2	Case3
SPI1	2	4	12
ZFP36L1	3	6	12
HDAC3	6	4	0

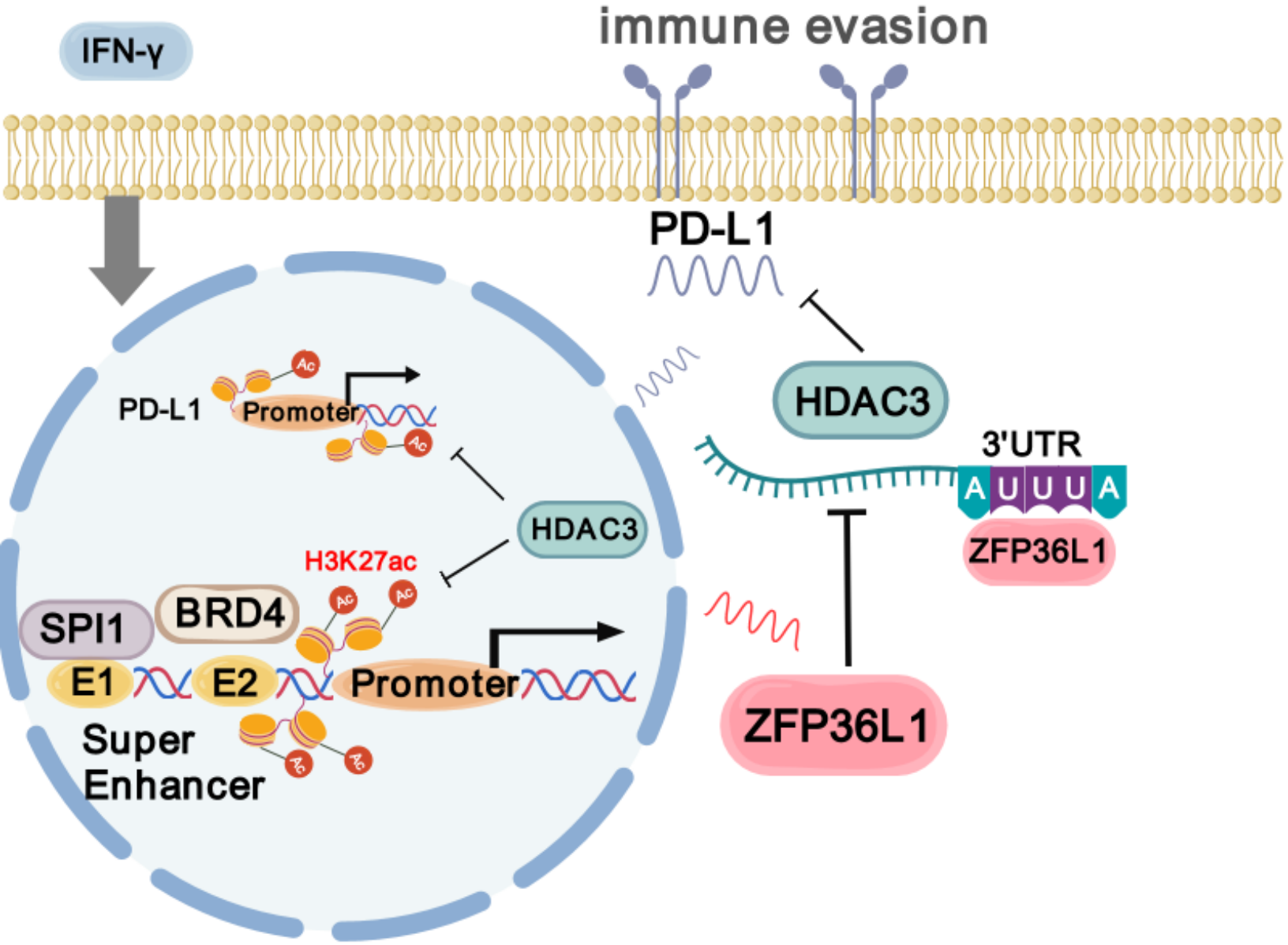
immune evasion
IFN-γ
PD-L1
HDAC3
3'UTR
A U U U A
ZFP36L1
PD-L1
Promoter
Ac
HDAC3
H3K27ac
SPI1
BRD4
E1
E2
Promoter
Super
Enhancer
ZFP36L1

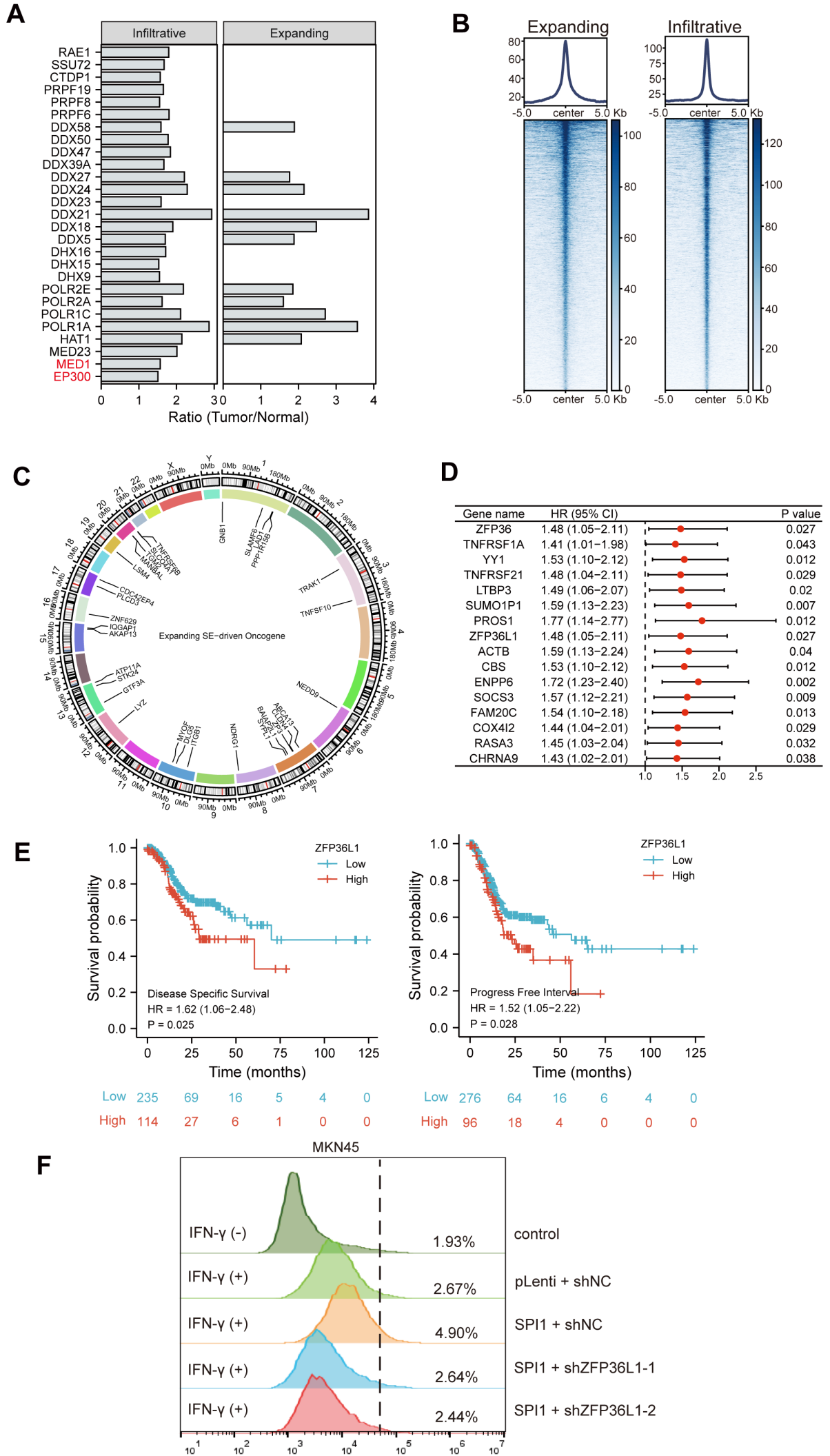
A
Infiltrative
Expanding
RAE1
SSU72
CTDP1
PRPF19
PRPF8
PRPF6
DDX58
DDX50
DDX47
DDX39A
DDX27
DDX24
DDX23
DDX21
DDX18
DDX5
DHX16
DHX15
DHX9
POLR2E
POLR2A
POLR1C
POLR1A
HAT1
MED23
MED1
EP300
Ratio (Tumor/Normal)
B
Expanding
Infiltrative
-5.0 center 5.0 Kb
C
Expanding SE-driven Oncogene
D
Gene name HR (95% CI) P value
ZFP36 1.48 (1.05−2.11) 0.027
TNFRSF1A 1.41 (1.01−1.98) 0.043
YY1 1.53 (1.10−2.12) 0.012
TNFRSF21 1.48 (1.04−2.11) 0.029
LTBP3 1.49 (1.06−2.07) 0.02
SUMO1P1 1.59 (1.13−2.23) 0.007
PROS1 1.77 (1.14−2.77) 0.012
ZFP36L1 1.48 (1.05−2.11) 0.027
ACTB 1.59 (1.13−2.24) 0.04
CBS 1.53 (1.10−2.12) 0.012
ENPP6 1.72 (1.23−2.40) 0.002
SOCS3 1.57 (1.12−2.21) 0.009
FAM20C 1.54 (1.10−2.18) 0.013
COX4I2 1.44 (1.04−2.01) 0.029
RASA3 1.45 (1.03−2.04) 0.032
CHRNA9 1.43 (1.02−2.01) 0.038
E
ZFP36L1
Low
High
Survival probability
Disease Specific Survival
HR = 1.62 (1.06−2.48)
P = 0.025
Time (months)
Low 235 69 16 5 4 0
High 114 27 6 1 0 0
Progress Free Interval
HR = 1.52 (1.05−2.22)
P = 0.028
Low 276 64 16 6 4 0
High 96 18 4 0 0 0
F
MKN45
IFN-γ (-) 1.93% control
IFN-γ (+) 2.67% pLenti + shNC
IFN-γ (+) 4.90% SPI1 + shNC
IFN-γ (+) 2.64% SPI1 + shZFP36L1-1
IFN-γ (+) 2.44% SPI1 + shZFP36L1-2

1.Table 1

GENE	5’ to 3’
GAPDH	Forward: ACAACTTTGGTATCGTGGAAGG
	Reverse: GCCATCACGCCACAGTTTC
ZFP36L1	Forward: ACCACCACCCTCGTGTCTG
	Reverse: TGCCCACTGCCTTTCTGT
CD274	Forward: TGGCATTTGCTGAACGCATTT
	Reverse: TGCAGCCAGGTCTAATTGTTTT
HDAC3	Forward: CCTGGCATTGACCCATAGCC
	Reverse: CTCTTGGTGAAGCCTTGCATA
SPI1	Forward: ATGGAAGGGTTTCCCCTCGT
	Reverse: CTGGAGCTCCGTGAAGTTGT
18S rRNA	Forward: GTCTGTGATGCCCTTAGATG
	Reverse: AGCTTATGACCCGCACTTAC
Mouse ZFP36L1	Forward: CACCCCAAGTACAAGACGGA
	Reverse: GCTAGGAGCAAAGAGGCTCG
Mouse CD274	Forward: GCTCCAAAGGACTTGTACGTG
	Reverse: TGATCTGAAGGGCAGCATTTC
ChIP-ZFP36L1-E1A	Forward: AAGTGCCAGTTTTCTTCCTTG
	Reverse: CACCAGTCCCTGCCAGTC
ChIP-ZFP36L1-E1B	Forward: CTAGCAAGGCCCTGGTATG
	Reverse: CTGTCCACATGGCAACCCT
ChIP-ZFP36L1-E1C	Forward: TTATACAACGTGGTGCTGGTG
	Reverse: GTGTCAGTGCCTCCTCATT
ChIP-ZFP36L1-E1D	Forward: GGAGGCACTGACACGGACA
	Reverse: GAATTCAAGTGGGGATTAGG
ChIP-CD274-P1	Forward: GCTGGGCCCAAACCCTATT
	Reverse: TTTGGCAGGAGCATG GAGTT
ChIP-CD274-P2	Forward: ATGGGTCTGCTGCTGACTTT
	Reverse: GGCGTCCCCCTTTCTGATAA
ChIP-CD274-P3	Forward: ACTGAAAGCTTCCGCCGATT
	Reverse: CCCAAGGCAGCAAAT CCAGT

2. Plasmid

pLenti-CMV-ZFP36L1-GFP-Puro

pcDNA3.1-ZFP36L1-Flag

pPLK-GFP-Puro-ZFP36L1 shRNA-1: GTAACAAGATGCTCAACTATA

pPLK-GFP-Puro-ZFP36L1 shRNA-2: CCTCCAGCATAGCTTTAGCTT

pcDNA3.1-mutZFP36L1-Flag (C153R-C173R)

pLVX-CMV-ZFP36L1(mouse)-3×Flag-Puro

pLKO.1-U6-ZFP36L1 shRNA-1(mouse)-EF1a-copGFP-T2A-Puro: GCTTTCGAG ACCGCTCTTTCTC

pLKO.1-U6-ZFP36L1 shRNA-2(mouse)-EF1a-copGFP-T2A-Puro: GCTGCCACTT CATTCATAACGC

pLenti-CMV-SPI1-GFP-Puro——ID：6688；NM_001080547.2

pLenti-CMV-ELF1-GFP-Puro——ID：1997；NM_172373.4

pLenti-CMV-E2F1-GFP-Puro——ID：1869；NM_005225.3

pcDNA3.1-BRD4-3×Flag

pGEX-4T-2-GST-SPI1

pET-32a-His-BRD4

pLVX-Puro-Flag-HDAC3

pGL4-Luci-E1 (Full length)——chr14:68806839-68807740

pGL4-Luci-E1A——chr14:68806839-68807000

pGL4-Luci-E1B——chr14:68807000-68807300

pGL4-Luci-E1C (Wild)——chr14:68807300-68807500

pGL4-Luci-E1C (Deletion)——chr14:68807300-68807469 + 68807483-68807500, deletion: GAAGAGGGAAGGCAG

pGL4-Luci-E1D——chr14:68807500-68807740

pGL4-Luci-CD274 promoter

pmirGLO-HDAC3-3'UTR (Wild)——"ATTTA" motif

pmirGLO-HDAC3-3'UTR (Mutant)——"ACCCA" mutant motif

3. Materials and Methods

3.1 Statistical methods

If the variable is numerical and the sample size is ≤5000, a normality test will be conducted. If the data follow a normal distribution, the mean ± standard deviation of the corresponding variable will be calculated; otherwise, the median (upper and lower quartiles) of the corresponding variable will be reported. For numerical variables that

satisfy the normal distribution and pass the variance chi-square test, two-group comparisons will be performed using the T-test, and three-group comparisons will use One-way ANOVA. If the data satisfy the normal distribution but fail the variance chi-square test, two-group comparisons will be conducted using Welch's t-test, and three-group comparisons will use Welch's one-way ANOVA. If the data do not satisfy the normal distribution assumption, two-group comparisons will use Welch's one-way ANOVA. For normally distributed data, two-group comparisons will use the Wilcoxon test, and three-group comparisons will use the Kruskal-Wallis test.

If the variables are categorical and the data satisfy the condition of theoretical frequency > 5 with a total sample size ≥ 40, group comparisons will use the chi-square test. When the data meet the condition of 1 ≤ theoretical frequency ≤ 5 and the total sample size ≥ 40, group comparisons will use the corrected chi-square test (Yates' correction). If the data do not meet the conditions of theoretical frequency <1 or total sample size <40, group comparisons will utilize Fisher's exact test.

3.2 Hematoxylin & eosin (HE) and immunohistochemical (IHC) staining

3.3.1 Tissue Preparation:

Fresh tissue specimens are immersed in formalin fixative solution and incubated overnight at 4°C on a shaker. Tissues are dehydrated using an automatic dehydration instrument, embedded in paraffin using a paraffin embedding machine, and stored as tissue blocks at -20°C. Tissue sections of 4 μm thickness are prepared using a microtome, followed by flattening, lifting, and drying in a dark place.

3.3.2 Deparaffinization:

Slides are baked at 65°C in a constant temperature chamber for 6-24 hours. Before staining, slides are deparaffinized to water. This involves sequential immersion in decreasing concentrations of ethanol: xylene substitute for 10 minutes, absolute ethanol for 2 minutes, 95% ethanol for 2 minutes, 75% ethanol for 2 minutes, and finally pure water, with each step repeated twice. For Hematoxylin-Eosin (HE) staining, slides are directly stained with hematoxylin for 3 minutes, followed by 10 seconds of decolorization in hydrochloric acid ethanol and rinsing in pure water for 5 minutes. Then, slides are stained with eosin for 30 seconds before proceeding to step

5 for mounting.

3.3.3 Antigen Retrieval:

Antigen retrieval is performed using high-pressure steam. Slides are placed in a metal dish filled with sodium citrate buffer solution and completely submerged. The dish is then placed in a preheated boiling pressure cooker and sealed. The heating plate is set to maximum power. Once the pressure cooker reaches maximum pressure and the valve releases steam for 2 minutes, the heating plate is turned off. After waiting for 30 minutes, the lid is opened, and the slides are cooled at room temperature for 2 hours.

3.3.4 Immunostaining:

Immunohistochemical experiments are conducted using an immunostaining kit. The specific steps are as follows: Wash the fixed sections with PBS solution for 3 minutes × 2 times, then rinse with PBS for the third time. Apply endogenous peroxidase blocker to the defined tissue area on the slide and incubate at room temperature for 10 minutes. Wash the slides with PBS for 3 minutes × 3 times, remove PBS, apply nonspecific staining blocker, and incubate at room temperature for 10 minutes. Apply primary antibody (diluted at 1:500) and incubate overnight at 4°C. Wash the slides with PBS for 3 minutes × 3 times, remove PBS, apply biotinylated goat anti-mouse/rabbit IgG polymer, and incubate at room temperature for 10 minutes. Wash the slides with PBS for 3 minutes × 3 times, remove PBS, apply streptavidin-horseradish peroxidase, and incubate at room temperature for 10 minutes. Apply freshly prepared DAB staining solution and incubate at room temperature for 2 minutes.

3.3.5 Mounting:

Slides are counterstained with hematoxylin, incubated at room temperature for 3 minutes, followed by decolorization in hydrochloric acid ethanol for 10 seconds, and then rinsed under running water for 15 minutes. Slides are dehydrated using a reverse deparaffinization process: 75% ethanol for 2 minutes, 95% ethanol for 2 minutes, absolute ethanol for 2 minutes, and finally xylene substitute for 5 minutes, with each step repeated twice. After thorough ventilation drying, slides are mounted with neutral

resin.

3.3.6 Immunohistochemistry Scoring:

The scoring is based on the staining extent of positive tumor cells in the tissue: <25% scores 1 point, 25%~50% scores 2 points, 50%~75% scores 3 points, and ≥75% scores 4 points. Staining intensity is scored as follows: no staining (0 points), weak positive (1 point), moderate positive (2 points), and strong positive (3 points). The final score is obtained by multiplying the scores of staining extent and intensity. High expression is defined as 5 points or above, while low expression is less than 5 points.

3.3 Real Time PCR

3.3.1 RNA Sample Preparation:

Total RNA extraction was conducted using a cell total RNA extraction kit. Specifically, 500 μL of Buffer RL was added to each well of a 6-well plate to lyse cells. After thorough cell lysis, the lysate was transferred to gDNA filter columns and centrifuged at 12000 rpm for 30 seconds to collect the filtrate. Subsequently, 250 μL of ethanol was added, mixed well, and transferred to RNA adsorption columns, followed by centrifugation at 12000 rpm for 30 seconds, and the flow-through was discarded. Washing steps were performed with 700 μL of Buffer RW1 and Buffer RW2, each followed by centrifugation and discarding of the flow-through. Finally, 500 μL of Buffer RW2 was added, centrifuged at 12000 rpm for 2 minutes, and the flow-through was discarded. The RNA adsorption column was transferred to a 1.5 mL centrifuge tube, and 50 μL of RNase-free ddH2O preheated to 65°C was added to the center of the column. After incubating at room temperature for 2 minutes, RNA was eluted by centrifugation at 12000 rpm for 1 minute, and the concentration was measured.

3.3.2 RNA Reverse Transcription:

Each sample tube containing 2 μg of RNA template was adjusted to a volume of 7 μL with DEPC water. The mixture was denatured at 65°C for 5 minutes and then chilled on ice for 2 minutes. Reverse transcription reactions were performed using the HiFi-MMLV cDNA first-strand synthesis kit. Each reaction was set up with 4 μL of dNTP Mix, 4 μL of 5×RT Buffer, 2 μL of Primer Mix, 2 μL of DTT, and 1 μL of

HiFi-MMLV. The thoroughly mixed 13 μL reaction mixture was added to 7 μL of RNA template, followed by incubation at 42°C for 50 minutes and then at 85°C for 5 minutes to complete reverse transcription.

3.3.3 Real-time Fluorescent Quantitative PCR (RT-PCR):

The obtained cDNA was diluted 2-fold for use as RT-PCR templates. Each reaction well was filled with 10 μL of 2×UltraSYBR Mixture, 0.6 μL each of upstream and downstream primers for the target gene, and 6.8 μL of ddH2O. After thorough mixing and centrifugation, 2 μL of diluted cDNA template was added to each reaction well, followed by the addition of 18 μL of the above mixed system. The RT-qPCR program consisted of three steps: initial denaturation at 95°C for 10 minutes, followed by 40 cycles of PCR amplification (95°C for 10 seconds, 60°C for 30 seconds, and 72°C for 32 seconds), and finally, a melting curve analysis (95°C for 15 seconds, 60°C for 60 seconds, 95°C for 15 seconds, and 60°C for 15 seconds).

3.4 RNA-binding protein immunoprecipitation

3.4.1 Sample Preparation:

MGC803 cells transfected with pcDNA3.1-ZFP36L1-Flag plasmid were washed with pre-chilled PBS at 4°C, harvested, and transferred to 1.5 mL EP tubes. After centrifugation at 1500 rpm for 5 minutes at 4°C, the supernatant was discarded. Each tube was resuspended in 250 μL of RIP lysis buffer, homogenized, and left on ice for 5 minutes. The collected cell lysates were stored at -80°C.

3.4.2 Magnetic Bead and Antibody Binding:

Fifty microliters of resuspended magnetic beads were added to each 1.5 mL EP tube, followed by the addition of 500 μL of RIP wash buffer. The tubes were vortexed and placed on a magnetic separator until the solution cleared, and the supernatant was discarded. The beads were washed again with RIP wash buffer. After resuspending the beads in 100 μL of RIP wash buffer, approximately 8 μg of Flag antibody or IgG was added to each tube, and incubated at room temperature for 30 minutes. The tubes were placed on a magnetic separator until the solution cleared, and the supernatant was discarded. The beads were washed again with RIP wash buffer.

3.4.3 RNA-binding protein immunoprecipitation:

Each tube was supplemented with 900 μL of RIP immunoprecipitation buffer. The cell lysates prepared in the first step were thawed, centrifuged at 14000 rpm for 10 minutes at 4°C, and a portion of the sample was retained as a 5% input control (Input) for direct RNA purification. One hundred microliters of the supernatant was added to the magnetic bead-antibody complex to make a total volume of 1 mL, and incubated overnight at 4°C. The tubes were placed on a magnetic separator, the supernatant was discarded, and the beads were washed six times with RIP wash buffer.

3.4.4 RNA Purification:

The immunoprecipitation complexes were resuspended in 150 μL of Proteinase K buffer and incubated at 55°C for 30 minutes. After placing the tubes on a magnetic separator, the supernatant was collected, and 250 μL of RIP wash buffer was added to each tube. Four hundred microliters of phenol-chloroform-isoamyl alcohol mixture was added, vortexed for 15 seconds, and centrifuged at 14000 rpm for 10 minutes at room temperature. The upper aqueous phase (350 μL) was carefully transferred to new EP tubes, and each tube was supplemented with 50 μL of Salt Solution I, 15 μL of Salt Solution II, 5 μL of Precipitate Enhancer, and 850 μL of ethanol. After incubating overnight at -80°C, the tubes were centrifuged at 14000 rpm for 30 minutes at 4°C, and the supernatant was discarded. The RNA pellet was washed with 80% ethanol, air-dried, and dissolved in 20 μL of DEPC-treated water.

3.4.5 RT-PCR Quantitative Analysis:

RNA was reverse transcribed into cDNA, and real-time fluorescent quantitative PCR was performed to detect the products. After normalizing the results with Input, fold differences were analyzed.

3.5 Co-immunoprecipitation

3.5.1 DYKDDDDK-G1 Affinity Resin:

Resin Pre-treatment: Take 50 μL of affinity resin slurry and place it in a 1.5 mL EP tube. Add 500 μL of TBS buffer, centrifuge at 6000 g for 30 seconds, discard the supernatant, and repeat the wash step twice. Resin-Sample Binding:Add 400 μL of prepared protein sample to the resin, mix thoroughly, and incubate overnight at 4°C

on a rotary mixer. Add 500 μL of TBS buffer, centrifuge at 6000 g for 30 seconds, discard the supernatant, and repeat the wash step twice. Denaturing Elution:Add 25 μL of Loading Buffer, mix well, heat at 100°C for 5 minutes, centrifuge at 6000 g for 30 seconds, collect the supernatant, and proceed with Western Blot detection.

3.5.2 Protein A/G Magnetic Bead Method:

Bead/Antibody Pre-treatment: Take 30 μL of magnetic beads and place them in a 1.5 mL EP tube. Add 400 μL of binding/washing buffer, mix well, magnetically separate, discard the supernatant, and repeat the wash step twice. Dilute the antibody with binding/washing buffer to a final concentration of 5 μg/mL. Antibody-Bead Binding: Add the diluted 400 μL antibody to the prepared beads, mix well, and incubate at 4°C for 2 hours on a rotary mixer. Magnetically separate, collect the beads, add 400 μL of binding/washing buffer, mix well, magnetically separate, discard the supernatant, and repeat the wash step twice. Antigen-Antibody-Bead Complex Binding: Add 400 μL of prepared antigen sample to the beads, mix well, and incubate at 4°C for 2 hours on a rotary mixer. Magnetically separate, collect the beads, add 400 μL of binding/washing buffer, and repeat the wash step twice. Denaturing Elution: Separate the beads, discard the supernatant, add 25 μL of Loading Buffer, mix well, heat at 95°C for 5 minutes, separate the beads, collect the supernatant, and proceed with Western Blot detection.

3.6 GST pull-down

3.6.1 Protein Prokaryotic Expression:

pET-32a-His-BRD4 plasmid, pGEX-4T-2-GST-SPI1 plasmid, and empty vector plasmid were transformed into competent cells. During the logarithmic growth phase of the cultured bacteria after 5 hours of shaking, isopropyl β-D-1-thiogalactopyranoside (IPTG) was added to a final concentration of 1 mmol/L to induce expression at 18°C for 24 hours. Additionally, 500 μL of bacterial culture was taken without induction and mixed with loading buffer for subsequent experimental controls. Bacterial pellets were collected by centrifugation, resuspended in PBS containing protease inhibitors, treated with lysozyme to a final concentration of 2 mg/mL at 4°C for 30 minutes, followed by sonication at 25% power for 1 minute

(3 seconds on, 3 seconds off, repeated 10 times) until clear. Centrifugation was performed at 15000 rpm for 15 minutes at 4°C.

3.6.2 His-BRD4 Protein Purification:

The cleared supernatant after centrifugation was added to Ni-NTA purification columns pre-equilibrated with PBS at a 10-fold column volume, and allowed to flow through naturally for 8 times. Gradient washing was performed using PBS containing 20 nM and 40 nM imidazole, followed by protein elution using PBS containing 250 nM imidazole. The purified protein was collected and stored at -80°C.

3.6.3 GST-SPI1 Protein Purification:

The cleared supernatant after centrifugation was incubated with GST beads for 1 hour, followed by centrifugation at 2000 g for 3 minutes, and discarding the supernatant. The GST beads were washed three times with 10-fold volume PBS, followed by elution with 1 mL GST Elution Buffer for 10 minutes, and centrifugation at 2000 g for 3 minutes. The eluate was collected, and the purification was repeated twice. The purified protein was stored at -80°C.

3.6.4 GST Pull-down Assay:

The GST pull-down assay was conducted using a GST pull-down kit, following the instructions provided. This included equilibration of glutathione resin, binding of the target protein expressed as GST fusion, preparation of prey protein, elution of bait-prey protein complex, and gel electrophoresis analysis.

3.7 RNA pull-down

3.7.1 Plasmid Construction and Transfection:

pcDNA3.1-ZFP36L1-Flag and pcDNA3.1-mutZFP36L1-Flag plasmids were transfected into MGC803 cells. After 48 hours, cells were harvested and lysed using lysis buffer.

3.7.2 RNA Probe Preparation:

The clone plasmid containing the HDAC3 probe sequence was transcribed into single-stranded RNA probes using T7 RNA polymerase. After phenol-chloroform purification, the RNA probes were biotinylated using the RNA 3’ End Biotinylation

Kit and incubated overnight at 16 ° C. RNA was then recovered using phenol-chloroform extraction and dissolved in DEPC-treated water.

3.7.3 RNA-Protein Pull-down Assay:

This assay includes pre-treatment of magnetic beads, binding of biotinylated RNA probes to streptavidin-coated magnetic beads, RNA-protein binding, washing and elution of the RNA-protein complex, positive probe controls, and Western blot analysis of the results.